AGU PUBLICATIONS

JGR

Journal of Geophysical Research: Space Physics

RESEARCH ARTICLE
10.1002/2016JA022863

Key Points:
- Fifty-four trailing edges are examined; a velocity bend signature chosen as the clearest indicator of location of the trailing-edge stream interface
- Differences are found at 1 AU between the leading and trailing edges that cannot be explained as rarefaction versus compression
- The possibility is explored that the differences in properties are owed to differences in the leading and trailing edges of coronal holes

Correspondence to:
J. E. Borovsky,
jborovsky@spacescience.org

Citation:
Borovsky, J. E., and M. H. Denton (2016), The trailing edges of high-speed streams at 1 AU, *J. Geophys. Res. Space Physics*, *121*, 6107–6140, doi:10.1002/2016JA022863.

Received 25 APR 2016
Accepted 21 JUN 2016
Accepted article online 24 JUN 2016
Published online 23 JUL 2016

The trailing edges of high-speed streams at 1 AU

Joseph E. Borovsky[1,2] and Michael H. Denton[1,3]

[1]Space Science Institute, Boulder, Colorado, USA, [2]Climate and Space Science and Engineering, University of Michigan, Ann Arbor, Michigan, USA, [3]New Mexico Consortium, Los Alamos, New Mexico, USA

Abstract The trailing-edge rarefactions of 54 high-speed streams at 1 AU are analyzed. The temporal durations of the trailing-edge rarefactions agree with ballistic calculations based on the observed speeds of the fast and slow wind bounding the rarefactions. A methodology is developed to measure solar-wind compression and rarefaction using the orientations of solar-wind current sheets. One focus is to determine the signature that best describes the location of the trailing-edge stream interface between coronal-hole-origin plasma and streamer-belt-origin plasma; based on the current-sheet orientations, on the magnetic-field strength, on the intensity of the electron strahl, and on the intensity of the negative vorticity, an inflection point in the temporal profile of the solar-wind velocity is taken as the best indicator of the trailing-edge stream interface. Computer simulations support this choice. Using superposed-epoch analysis, the plasma properties and turbulence properties of trailing-edge rarefactions are surveyed. Whereas the signatures of the coronal-hole/streamer-belt (slow-wind/fast-wind) boundary in the leading edge (corotating interaction region) stream interface are simultaneous, they are not simultaneous in the trailing edge, with ion-charge-state signatures occurring on average 13.7 h prior to the proton entropy signature. It is suggested that differences in the leading and trailing edges of coronal holes on the Sun might account for the differences in the leading and trailing edges of high-speed streams at 1 AU: the formation timescales, heating timescales, and charge-state-equilibration timescales of closed flux loops in the corona might be involved.

1. Introduction

Because the rotating Sun has regions on its surface that produce wind of different speeds, along a radial line outward from the Sun will be regions of radially outflowing slow wind and regions of radially outflowing fast wind. On the leading (outward) edge of a region of high-speed wind (a high-speed stream) the faster solar wind rams into slower solar wind and forms a region of plasma compression (a corotating interaction region, CIR); on the trailing (inward) edge of a high-speed stream the fast wind outruns the slow wind and forms a region of plasma rarefraction. The fast solar wind has its origin from coronal holes on the Sun; the slow solar wind has its origin from streamer belts and streamer stalks on the Sun. In the CIRs on the leading edges of the high-speed streams there is a well-known sharp boundary making the transition from streamer-belt-origin plasma into coronal-hole-origin plasma known as the "CIR stream interface." By symmetry, in the trailing-edge rarefaction there should be another stream interface making the transition from coronal-hole-origin plasma into streamer-belt-origin plasma: the "trailing-edge stream interface".

Corotating interaction regions have been well studied [*Hundhausen*, 1973; *Richter and Luttrell*, 1986; *Pizzo*, 1989, 1991; *Crooker and Gosling*, 1999; *Jian et al*., 2006; *Tessein et al*., 2011], in part because CIRs drive geomagnetic storms [*Denton et al*., 2006; *Tsurutani et al*., 2006; *Borovsky and Denton*, 2006, 2013; *Richardson et al*., 2006; *Lavraud et al*., 2006; *Solomon et al*., 2012]. The trailing edges of high-speed streams are less studied [*Carovillano and Siscoe*, 1969; *Tu and Marsch*, 1995; *Gosling and Pizzo*, 1999; *Pagel et al*., 2004; *Ko et al*., 2006]: the trailing edges of high-speed streams drive the latter portions of high-speed-stream-driven geomagnetic storms wherein geomagnetic activity is subsiding, but the Earth's electron radiation belt is still being energized [*Tsurutani et al*., 1995; *McPherron et al*., 2009; *Borovsky and Denton*, 2010a, 2010b]. The CIR stream interface on the leading edges of high-speed streams has been well characterized [e.g., *Burlaga*, 1974; *Gosling et al*., 1978; *Crooker and Gosling*, 1999; *Forsyth and Marsch*, 1999; *Intriligator et al*., 2001; *Simunac et al*., 2009; *Crooker et al*., 2010; *Borovsky and Denton*, 2010c; *Crooker and McPherron*, 2012]. To identify the stream interface in leading-edge CIRs, various signatures have been utilized: the reversal of the east-west flow deflection of the solar wind [*Gosling et al*., 1978; *McPherron and Weygand*, 2006], the peak of the total (magnetic field plus thermal) pressure [*Jian et al*., 2006], a sudden increase in the proton specific entropy [*Siscoe and Intriligator*, 1993; *Lazarus et al*., 2003], a sudden change in the heavy-ion composition and in the

FIP (first ionization potential) elemental abundance [*Wimmer-Schweingruber et al*., 1997; *Crooker and McPherron*, 2012], or the peak in the plasma vorticity [*Borovsky and Denton*, 2010c]. Discussion of the stream interface in the trailing-edge rarefaction is quite limited [*Burlaga et al*., 1990; *Geiss et al*., 1995; *Burton et al*., 1999; *Zurbuchen et al*., 1999; *Kahler*, 2010; *Simunac et al*., 2010]. The most extensive study of the trailing-edge stream interface is that of *Burton et al*. [1999], who examined 18 recurrences of a single persistent high-speed stream at 13–36° of latitude and 4.5–5 AU in distance from the Sun in the years 1992–1993. They recommend identifying the trailing-edge stream interfaces with a sharp drop in the proton specific entropy S_p. They also found that drops in the proton specific entropy, jump increases in the Mg/O elemental density ratio, jump increases in the oxygen charge-state ratio, and drops in the alpha-to-proton density ratio were all temporally coincident. *Geiss et al*. [1995] also found abrupt signatures in the trailing edge that were simultaneous. Contrary to this, *Zurbuchen et al*. [1999] found the oxygen charge-state ratios to have gradual transitions across the trailing edges rather than jump increases; *Simunac et al*. [2010] also reported less distinct changes in the trailing-edge rarefaction than in the leading-edge CIR, as did *Pagel et al*. [2004]. The present study at 1 AU will find that the various candidate signatures for identifying the stream interface are typically not simultaneous and the present study will recommend a different signature to identify the location of the trailing-edge stream interface.

Note that the "trailing edge of a high-speed stream" should not be confused with the "CIR trailing edge" or "compression-region trailing edge" [cf. *Richardson*, 1985; *Lucek and Balogh*, 1998; *Ebert et al*., 2012].

In the present study 54 high-speed-stream trailing edges are examined at 1 AU in the years 1998–2008. The focus will be to (1) locate the stream interface in the trailing-edge rarefaction, (2) to find a signature that can identify the stream interface, and (3) to survey the properties of trailing-edge rarefactions in general and in comparison with the properties of leading-edge CIRs. This study will use data from OMNI2, ACE, Wind, and Stereo A + B and the data interpretation will be aided by 3-D global-MHD simulations and by 1-D fluid simulations.

Data sets utilized in this study are OMNI2 [*King and Papitashvili*, 2005], ACE SWEPAM [*McComas et al*., 1998], ACE MAG [*Smith et al*., 1998], Wind SWE [*Ogilvie et al*., 1995; *Kasper et al*., 2006], Wind 3DP [*Lin et al*., 1995], Wind Mag [*Lepping et al*., 1995], Stereo PLASTIC [*Galvin et al*., 2008], and ACE SWICS [*Gloeckler et al*., 1998].

This paper is organized as follows. In section 2 expectations for the properties of trailing edges of high-speed streams as compared to the properties of corotating interaction regions on the leading edges are explored. In section 3 the event selection criteria and the collection of 54 high-speed-stream trailing edges are discussed. In section 4 superposed-epoch analysis (with the help of computer simulations) is used to determine the best signature that identifies the stream interface in the trailing-edge rarefaction. In section 5 superposed-epoch analysis is used to explore the properties of high-speed-stream trailing edges in comparison with high-speed-stream leading edges. Section 6.1 discusses whether the initial velocity drop at the end of the high-speed stream is the beginning of the trailing-edge rarefaction or whether the trailing-edge rarefaction commences earlier in time. Section 6.2 discusses the possibility that the differences between the leading-edge and trailing-edge stream interfaces at 1 AU have their origins in differences between the leading and trailing edges of coronal holes on the Sun. The findings of this study are summarized in section 7, and a summary sketch of the chronology of signatures in the leading and trailing edges is presented. In Appendix A the methodology of measuring the amount of plasma compression or rarefaction in the solar wind with the orientations of current sheets in the plasma is discussed.

2. The Trailing Edges of High-Speed Streams

Figure 1 sketches the leading edge (left) and trailing edge (right) of a high-speed stream in the ecliptic plane as viewed from above the plane. The RTN coordinate system is noted in the bottom right of each sketch. In both cases the structures sketched move upward with time radially outward from the Sun. In both sketches a green dashed line indicates the path of the Earth through the structure as the structure moves radially outward from the Sun past the Earth, with the Earth moving in the figure temporally from top to bottom along the line. In Figure 1 (left) a blue dashed line indicates the location of the CIR stream interface, which is a Parker-spiral-oriented interface between streamer-belt plasma (slow wind) and coronal-hole-origin plasma (fast wind). Shaded in orange is the corotating interaction region (CIR), a region of compressed

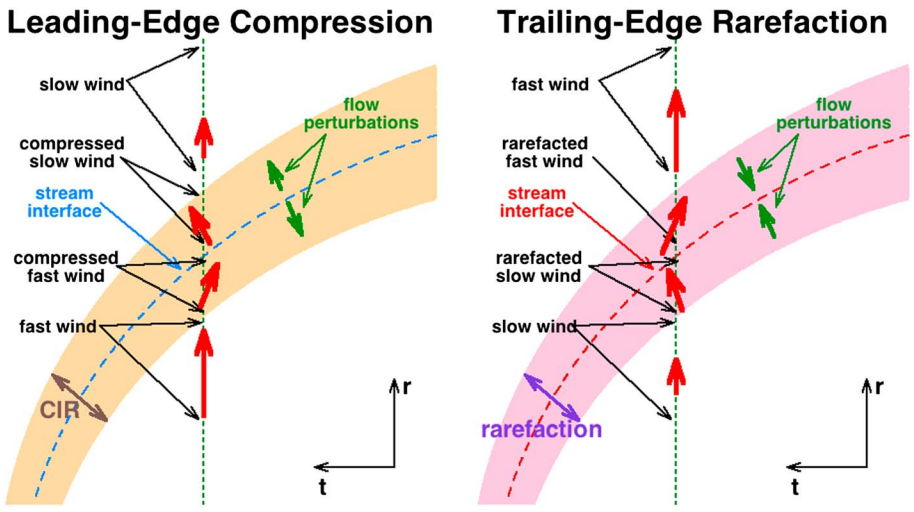

Figure 1. (left) A sketch of the compression (CIR) on the leading edge of a high-speed stream and (right) a sketch of the rarefaction on the trailing edge of a high-speed stream. Both sketches are drawn in the ecliptic plane with the RTN coordinate system indicated in the lower right.

plasma caused by the fast wind overtaking the slow wind. The corotating interaction region outward from the stream interface is compressed slow-wind plasma and the corotating interaction region inward of the stream interface is compressed coronal-hole-origin plasma (fast wind). The width of the CIR is related to the magnetosonic speeds in the fast and slow wind and the age of the CIR. Nominally in the unperturbed slow and fast wind, the velocity vectors (drawn in red) are radially outward from the Sun. Within the CIR there is a pressure-driven velocity perturbation perpendicular to the Parker spiral: this perturbation is indicated in the sketch by the green arrows pointing outward from the stream interface. Within the CIR this velocity perturbation deflects the radially flowing fast wind into the $-T$ direction and the radially flowing slow wind into the $+T$ direction. This is the well-known westward-then-eastward temporal flow deflection of

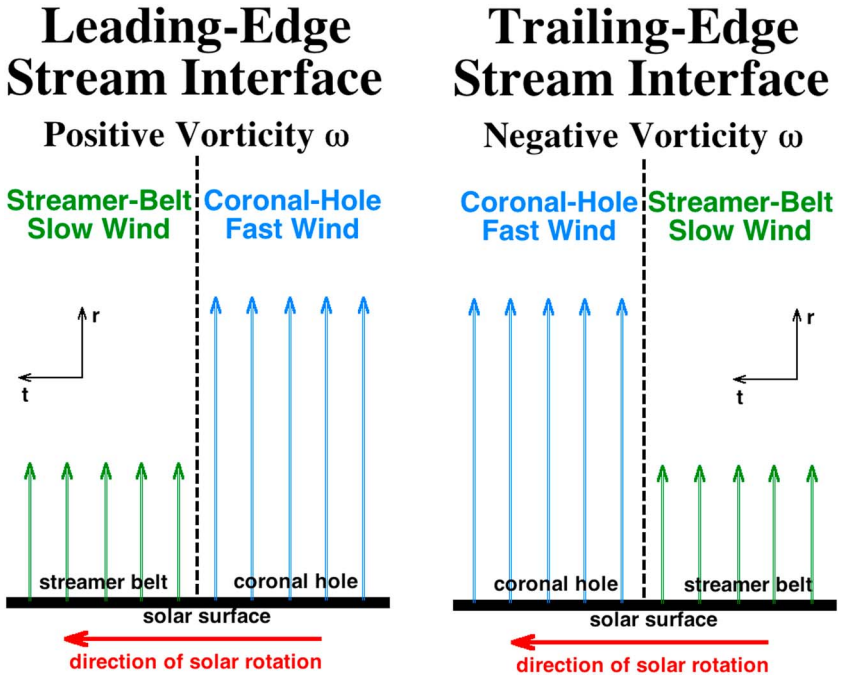

Figure 2. Two sketches of the streamer-belt/coronal-hole boundaries at the Sun. (left) The boundary at the westward leading edge of a coronal hole and (right) the boundary at the eastward trailing edge of a coronal hole. The RTN coordinate system is indicated in the sketches.

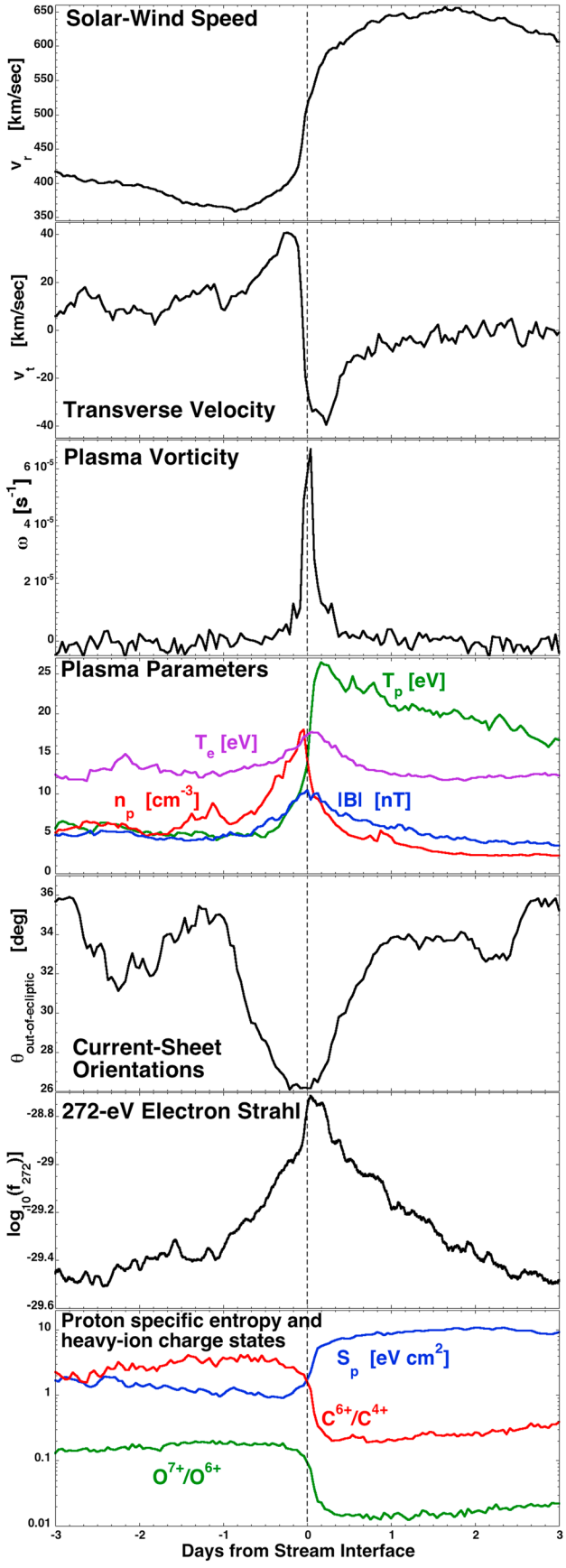

a CIR passing over the Earth [e.g., *Siscoe et al.*, 1969; *Belcher and Davis*, 1971]. The CIR is a large-scale pressure perturbation, not a large-scale shear zone [*Borovsky and Denton*, 2010c]. There is a narrow, intense velocity shear (vorticity layer) at the stream interface, which is a relic from the Sun. In Figure 2 (left) the creation of this vorticity layer at the fast-wind slow-wind boundary at the Sun is sketched. The stream interface is depicted as the vertical dashed black line, with slow wind (streamer-belt plasma and the sector-reversal-region plasma) to its left and fast wind (coronal-hole-origin plasma) to its right. The solar rotation is toward the left. Because of the change in the velocity across the stream interface, there is a vorticity $\omega = \nabla \times \underline{v}$ across the stream interface. In the RTN coordinate system (noted on the sketch), the vorticity vector ω is in the positive N direction.

In Figure 3 superposed-epoch averages of various quantities are plotted versus time for 27 leading-edge CIRs, with the zero epoch for the averaging being the time at which the stream-interface vorticity layer in each CIR reaches the ACE spacecraft. The 27 CIRs are from the collection utilized in *Borovsky and Denton* [2010c], where the event-selection criteria are discussed in detail. In Figure 3 (first panel) the solar-wind speed v_r as measured by ACE SWEPAM is plotted; the slow wind prior to the stream interface followed by fast wind afterward is seen. In Figure 3 (second panel) the transverse flow velocity v_t is plotted: the positive

Figure 3. Superposed averages of measurements for the 27 CIR events are plotted. The zero epoch (vertical dashed line) is the passage of the CIR stream interface as identified with the vorticity peak. From top to bottom, (first panel) the solar-wind speed (OMNI), (second panel) the transverse velocity of the solar wind (OMNI), (third panel) the plasma vorticity (ACE SWEPAM), (fourth panel) the plasma number density (OMNI), proton temperature (OMNI), magnetic-field strength (OMNI), and electron temperature (Wind 3DP), (fifth panel) the out-of-ecliptic angles of the current-sheet normal vectors (ACE Mag), (sixth panel) intensity of the 272-eV electron strahl (ACE SWEPAM), and (seventh panel) the proton specific entropy (OMNI), the carbon charge-state-density ratio (ACE SWICS), and the oxygen charge-state ratio (ACE SWICS).

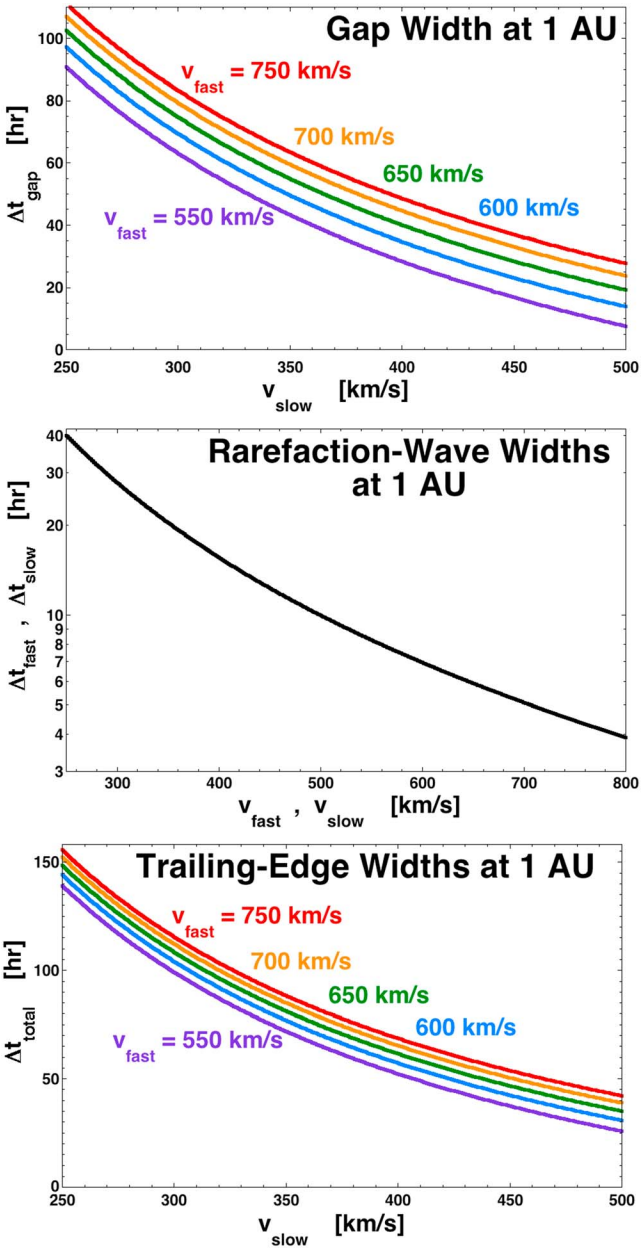

Figure 4. (top) The estimated temporal widths at 1 AU (from expression (1)) of the ballistic gap between the back of a high-speed stream and the front of an interval of slow solar wind. (middle) The estimated temporal widths at 1 AU (from expressions (2)) of a pressure-driven rarefaction into either the back of a high-speed stream or the front of an interval of slow wind. (bottom) The total temporal width of a rarefaction perturbation at 1 AU as given by expression (3).

v_t then negative v_t perturbation across the CIR is seen. In Figure 3 (third panel) the N component of the plasma vorticity $\omega = \nabla \times \underline{v}$ is plotted: note the sharp localized peak at the stream interface. In Figure 3 (fourth panel) the proton number density n_p, the proton temperature T_p, and the magnetic-field strength B_{mag} are plotted. Since B_{mag} has about the same average value in coronal-hole-origin plasma (4.7 nT for the collection of flattop high-speed streams at 1 AU [cf. *Borovsky*, 2016, Table 4]) and in streamer-belt plasma (6.2 nT for the collection of pseudostreamer slow wind in *Xu and Borovsky* [2015]), the quantity B_{mag} is a good indicator of the amount of compression or rarefaction that the solar-wind plasma has undergone. Note the increase (compression) of B_{mag} within the CIR in Figure 3 (fourth panel), peaking at the stream interface. In Figure 3 (fourth panel) the proton number density is also compressed within the CIR, but its value is not reliable as a measure of the amount of compression because of the presence of "noncompressive density structures" [*Gosling et al.*, 1981; *Borrini et al.*, 1981] inside the CIR. These density structures are owed to the presence of sector-reversal-region plasma in the CIR [*Xu and Borovsky*, 2015], which occurs in helmet-streamer CIRs but not in pseudostreamer CIRs. Another measure of compression is to look at the anisotropy of the current-sheet orientations in the plasma, with the microscale magnetic structure of the solar-wind plasma flattening under compression and stretching under rarefaction. As developed in Appendix A, compression or rarefaction can be discerned by looking at the statistics of the directions of the current-sheet normal vectors in the plasma as the current sheets are advected past a measuring spacecraft. The normal direction $\underline{n}$ of each current sheet is determined using the cross-product method [*Burlaga and Ness*, 1969; *Knetter et al.*, 2004] on the magnetic-field vector change across the current sheet via $\underline{n} = \underline{B}_1 \times \underline{B}_2 / |\underline{B}_1 \times \underline{B}_2|$ where $\underline{B}_1$ and $\underline{B}_2$ are the magnetic-field vectors on the two sides of the current sheet. For Figure 3 only strong current sheets that had magnetic-field direction changes $\Delta\theta_B > 40^o$ across them were used to calculate the normal directions. If, in RTN coordinates, the normal has components (n_r, n_t, n_n), then the out-of-ecliptic angle of the normal can be defined as $\theta_{\text{out-of-ecliptic}} = \arctan(|n_n|/(n_r^2 + n_t^2)^{1/2})$. As discussed in Appendix A, there is a reduction in the mean out-of-ecliptic angle $\theta_{\text{out-of-ecliptic}}$ of the normals when the solar-wind plasma is compressed in the radial and/or

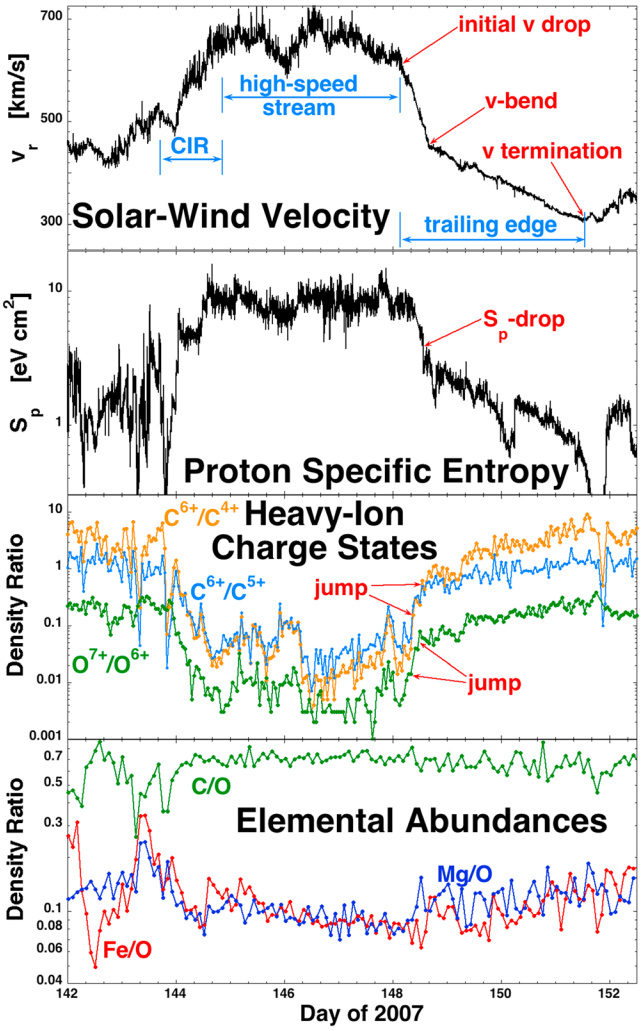

Figure 5. Over a time period of 10.5 days several relevant solar-wind parameters are plotted for Trailing Edge # 45 of Table 1 and for the high-speed stream that precedes the trailing edge. From top to bottom, (first and second panels) measurements from Wind SWE and (third and fourth panels) measurements from Ace SWICS.

tangential direction: such a decrease is seen around time $t = 0$ in the superposed average of the current-sheet normal angle in Figure 3 (fifth panel). In Figure 3 (sixth panel) the superposed average of the intensity of the 272-eV electron strahl as measured by ACE SWEPAM is plotted. In this panel the strahl intensity peaks just after the stream interface, as was reported by *Crooker et al.* [2010]. One possible explanation for this peak near the stream interface given by *Crooker et al.* [2010] is that the strahl is propagating from the Sun through a region of maximum compression where the solar-wind magnetic-field lines are closest together and this closeness of the field lines preserves the intensity of the electron strahl. (If that is the case, as a corollary we should expect the strength of the electron strahl to be a minimum at the trailing-edge stream interface where the rarefaction is the greatest, the field lines are farthest apart, and the strahl intensity is diluted the most.) In Figure 3 (seventh panel) the changes in the proton specific entropy $S_p = T_p/n_p^{2/3}$ and the heavy-ion charge-state-density ratios C^{6+}/C^{4+} and O^{7+}/O^{6+} are plotted: the transition in S_p is an increase from streamer belt (and sector reversal region) plasma into coronal-hole-origin plasma and the charge-state ratios decrease from streamer-belt (and sector-reversal-region) plasmas into coronal-hole-origin plasma.

In Figure 1 (right) the expectations for the trailing edge of a high-speed stream are sketched. Here fast wind leads slow wind and a Parker-spiral-oriented rarefaction occurs as the fast wind advects away from the slow wind: the rarefaction is shaded in pink. Somewhere within the rarefaction is a Parker-spiral-oriented stream interface separating the coronal-hole-origin plasma from the streamer-belt-origin plasma: this stream interface is sketched as the red dashed line. As will be found in section 4, identifying the stream interface in the trailing-edge rarefaction is not straightforward. In the rarefaction there is a pressure-driven velocity perturbation perpendicular to and toward the Parker-spiral-oriented stream interface. This velocity perturbation is sketched as the green arrows in Figure 1 (right). Ahead (outward) of the stream interface, the velocity perturbation turns the radial flow of the fast coronal-hole-origin plasma into the $-T$ direction, and behind (inward) the stream interface it turns the radial flow of the slow streamer belt plasma into the $+T$ direction. For Earth moving down the green dotted line through this pattern there will be an eastward-then-westward flow perturbation, opposite to the transverse flow temporal pattern in a CIR.

The difference in the radial velocities of the fast wind and the slow wind will ballistically leave a Parker-spiral-aligned gap between the fast plasma and the slow plasma. This gap will partially fill from pressure-driven expansion of plasma and field from both the fast and slow plasmas into the gap. The expansion flows will

Table 1. The Collection of 54 High-Speed-Stream Trailing Edges[a]

Event #	Year	Initial Velocity Drop (day of year)	Velocity-Bend (day of year)	Termination (day of year)	v_{fast} (km/s)	v_{slow} (km/s)	Type	Δt_{total} (h)
1	1998	303.29	303.70	305.80	578	367	HS	60.1
2	1999	298.88	299.76	?	557	?	HS	?
3	2000	30.33	33.12	36.55	?	371	HS	149.3
4	2000	345.41	348.79	351.13	643	312	HS	137.3
5	2001	201.00	201.75	203.41	577	361	HS	57.9
6	2002	66.21	67.58	70.46	615	358	PS	102.1
7	2002	92.59	95.00	96.62	667	328	PS	96.7
8	2003	135.38	137.87	138.62	697	404	HS	77.8
9	2003	162.63	163.42	164.50	670	394	HS	44.9
10	2003	250.04	250.41	251.50	560	376	PS	35.0
11	2003	255.96	256.75	258.50	601	351	HS	61.0
12	2003	268.79	270.46	273.04	691	293	HS	102.0
13	2003	349.50	350.87	353.96	750	304	HS	107.2
14	2004	64.50	64.79	67.92	579	318	HS	82.0
15	2004	336.46	337.75	340.17	655	295	HS	89.0
16	2004	353.84	354.84	356.09	585	348	HS	54.0
17	2005	24.00	25.25	27.38	667	323	HS	81.2
18	2005	41.63	?	44.96	717	361	HS	79.9
19	2005	62.17	62.96	64.08	622	377	HS	46.0
20	2005	69.58	71.46	72.79	665	323	HS	77.1
21	2005	96.29	97.38	99.37	593	318	DBL	73.8
22	2005	177.25	178.20	179.00	592	374	HS	42.0
23	2005	?	230.63	233.46	669	371	HS	?
24	2005	284.25	285.00	288.42	619	298	HS	100.1
25	2005	311.58	312.46	315.00	626	348	HS	82.1
26	2005	338.08	339.95	343.67	675	263	HS	133.9
27	2006	81.33	82.75	85.46	613	338	HS	99.2
28	2006	100.58	102.21	102.71	670	382	HS	51.0
29	2006	113.62	114.50	118.00	547	323	?	105.1
30	2006	134.04	135.25	137.29	585	319	HS	78.1
31	2006	154.54	155.00	157.08	570	323	HS	61.0
32	2006	187.95	?	190.79	567	330	HS	68.2
33	2006	215.75	216.67	218.96	527	331	HS	77.0
34	2006	303.63	304.41	307.38	559	333	HS	90.0
35	2006	316.38	317.62	319.63	590	347	HS	77.9
36	2006	?	361.04	362.50	?	328	HS	?
37	2007	46.79	49.87	55.26	684	268	HS	203.4
38	2007	60.96	61.96	62.71	600	340	HS	42.0
39	2007	66.75	68.25	70.25	625	298	HS	84.0
40	2007	93.87	95.46	98.84	583	295	HS	119.2
41	2007	102.55	103.83	106.87	524	310	HS	103.8
42	2007	120.50	122.71	126.88	646	266	HS	153.0
43	2007	129.67	130.08	133.87	587	299	HS	100.9
44	2007	140.29	?	142.71	620	420	HS	58.0
45	2007	148.17	148.75	151.54	629	305	HS	81.0
46	2007	293.92	294.67	298.25	664	340	PS	104.0
47	2007	330.33	331.71	334.67	631	329	HS	104.2
48	2007	347.83	?	350.80	557	350	HS	71.2
49	2007	357.16	358.25	360.29	601	333	HS	75.2
50	2008	35.25	36.08	38.54	617	336	HS	79.1
51	2008	62.04	64.17	67.88	754	316	HS	140.2
52	2008	127.32	?	133.79	644	304	PS	155.3
53	2008	197.62	200.82	202.46	647	288	HS	116.2
54	2008	206.34	206.71	209.17	646	341	PS	68.0

[a]The first column is the event number, second column the year, third column the time of the initial velocity drop, fourth column the time of the velocity-bend, fifth column the time of the velocity-decline termination, sixth column the speed of the fast wind in the high-speed stream, seventh column the speed of the solar wind at the time of termination, eighth column the type of streamer belt [HS = helmet streamer (one sector reversal), PS = pseudostreamer (no sector reversal), DSR = double sector reversal (two sector reversals)], and the ninth column is the total time duration of the rarefaction (termination time minus time of initial velocity drop).

be normal to the Parker-spiral direction and are seen as the transverse flow deflections v_t of the trailing edge. Simple time-of-flight arguments along a radial line can be used to estimate the temporal width of the gap as seen by a spacecraft at 1 AU. If the stream interface on the rotating Sun crosses the radial line connecting a spacecraft to the Sun at time $t = 0$, then the back edge of the fast wind will arrive ballistically at the satellite at time $t_{fast} = r_o/v_{fast}$ and the front edge of the slow wind will ballistically arrive at the spacecraft at time $t_{slow} = r_o/v_{slow}$, where $r_o = 1$ AU and where the v_{fast} and the v_{slow} are the speeds of the fast and slow wind, respectively. The difference $t_{slow} - t_{fast}$ in these two arrival times is the temporal width Δt_{gap} of the gap between the slow wind and the fast wind:

$$\Delta t_{gap} = r_o\left(v_{slow}{}^{-1} - v_{fast}{}^{-1}\right). \quad (1)$$

In Figure 4 (top) Δt_{gap} is plotted as a function of v_{slow} for five different values of v_{fast} (colors). The trailing-edge rarefaction between the fast and slow wind will be larger than this gap owing to the rarefaction waves that propagate into the fast and slow plasmas as those plasmas expand into the gap. Not accounting for the variation in the Parker-spiral orientation with distance from the Sun, and not accounting for the variation in the magnetosonic speed with distance from the Sun, the spatial widths of the rarefaction waves into the fast and slow plasmas at 1 AU are estimated as $L_{fast} = C_{ms\text{-}fast}t_{fast} = C_{ms\text{-}fast}r_o/v_{fast}$ and $L_{slow} = C_{ms\text{-}slow}t_{slow} = C_{ms\text{-}slow}r_o/v_{slow}$, where $C_{ms\text{-}fast}$ and $C_{ms\text{-}slow}$ are the magnetosonic speeds in the fast and slow plasmas. These spatial widths L_{fast} and L_{slow} at 1 AU pass the spacecraft in the times

$$\Delta t_{fast} = L_{fast}/v_{fast} = C_{ms\text{-}fast}r_o/v_{fast}{}^2 \quad (2a)$$

$$\Delta t_{slow} = L_{slow}/v_{slow} = C_{ms\text{-}slow}r_o/v_{slow}{}^2. \quad (2b)$$

For both the fast and the slow plasma at 1 AU, $C_{ms\text{-}fast} \sim C_{ms\text{-}slow} \sim 60$ km/s. For 60 km/s, Δt_{fast} and Δt_{fast} are plotted in Figure 4 (middle) as a function of v_{fast} or v_{slow}. The total temporal width of a trailing edge Δt_{trail} is the sum of the three widths:

$$\Delta t_{trail} = \Delta t_{gap} + \Delta t_{fast} + \Delta t_{slow}. \quad (3)$$

In Figure 4 (bottom) Δt_{trail} is plotted as a function of v_{slow} for five values of v_{fast} (colors).

As was the case for the CIR stream interface, there is a vorticity at the trailing-edge stream interface. In Figure 2 (right) the origin of this vorticity at the Sun is depicted. With the fast wind to the left of the stream interface (dashed black line) and the slow wind to the right, the vorticity vector $\omega = \nabla \times \underline{v}$ in the RTN coordinates system (noted on the sketch) is in the $-N$ direction. At 1 AU, negative vorticity at the trailing-edge stream interface is anticipated.

In Figure 5 a high-speed stream and its leading and trailing edges are plotted. In Figure 5 (first panel) the solar-wind flow v_r is plotted as a function of time as measured by Wind SWE: The high-speed stream is indicated in red, as is the CIR (slow-wind to fast-wind transition) and the trailing edge (fast-wind to slow-wind transition). In Figure 5 (first panel) two important features of the trailing edge are denoted. The first is the initial drop of the velocity: this is probably the leading edge of the rarefaction propagating into the coronal-hole-origin plasma at the local magnetosonic speed. The second feature is the distinct bend of the velocity profile to a decreasing temporal slope. The "*v*-bend" will be a candidate indicator of the location of the stream interface in the trailing edge. In Figure 5 (second panel) the proton specific entropy $S_p = T_p/n_p{}^{2/3}$ of the solar-wind plasma is plotted logarithmically. A sharp drop of S_p is seen within the trailing edge near the location of the velocity-bend. In Figure 5 (third panel) the heavy-ion charge-state-density ratios C^{6+}/C^{4+}, C^{6+}/C^{5+}, and O^{7+}/O^{6+} are plotted as measured by ACE SWICS: clear simultaneous upward jumps of C^{6+}/C^{4+}, C^{6+}/C^{5+}, at O^{7+}/O^{6+} are seen. These jumps in C^{6+}/C^{4+}, C^{6+}/C^{5+}, at O^{7+}/O^{6+} occur prior to the drop in S_p, while S_p remains at the value in the high-speed stream. In general, the downward drops of S_p are more sudden than the upward jumps of C^{6+}/C^{4+}, C^{6+}/C^{5+}, and O^{7+}/O^{6+}. In Figure 5 (fourth panel) the elemental density ratios C/O, Mg/O, and Fe/O are plotted as measured by ACE SWICS. An Mg/O increase and a Fe/O increase can be seen in Figure 5 (fourth panel).

3. Event Selection

A collection of 54 high-speed-stream trailing-edge rarefactions of high-speed streams is gathered by examining the solar wind in 1998–2008 using the OMNI2, ACE SWEPAM, and ACE SWICS data sets.

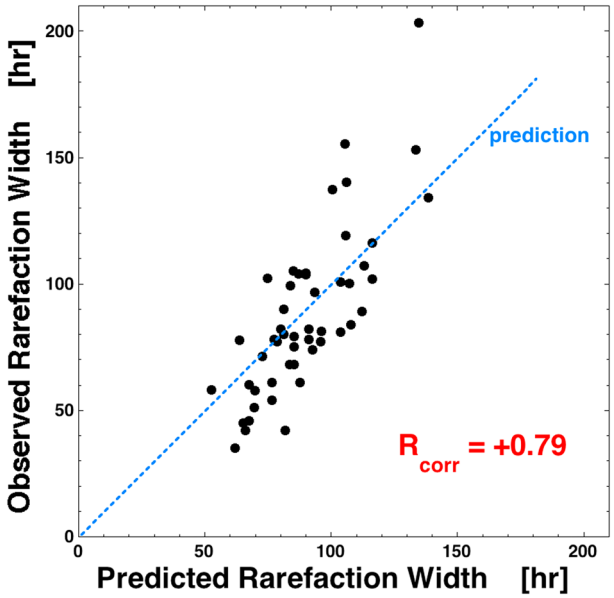

Figure 6. For the trailing edges listed in Table 1, the observed temporal width at 1 AU of each trailing edge is plotted vertically versus the predicted trailing-edge width from expression (3) using the measured velocities of the slow and fast wind bounding each trailing edge. The dashed blue curve (not a fit) indicates where observation would match prediction.

Four selection criteria are used to accept a trailing edge into the collection. The first criterion is that the trailing edge must be preceded by a robust high-speed stream with a duration of a day or more. Flattop high-speed streams [*Borovsky*, 2016] are preferred. Second, a trailing edge is rejected if its temporal velocity profile is irregular. Profiles that are quasi-monotonic without discontinuities or multiple bend points are chosen. Third, a trailing edge is rejected if it contains clear signatures of ejecta. These signatures include depressed proton temperatures [*Gosling et al.*, 1973; *Elliott et al.*, 2005], long-duration out-of-ecliptic magnetic-field vectors [*Lepping et al.*, 2005; *Borovsky*, 2010], or bidirectional strahl [*Gosling et al.*, 1987; *Richardson and Cane*, 2010]. The fourth criterion is that the velocity within the trailing edge should eventually reach low speeds (~400 km/s or less). That is, the high-speed stream following the trailing edge cannot be too close in time to the high-speed stream preceding the trailing edge.

The collection of 54 high-speed-stream trailing edges appears in Table 1. For each trailing edge, the start time (determined from the initial velocity drop at the end of the high-speed stream), the termination time (determined as the point where the solar-wind velocity ceases to decline or starts to increase), the time of the velocity inflection or "velocity-bend," and the total time duration of the trailing edge (from the initial velocity drop to the termination). Also noted in Table 1 is the helmet-streamer versus pseudostreamer nature of the streamer-belt plasma in the trailing edge.

The total time durations of the trailing edges are listed in the final column of Table 1: the mean value and standard deviation of the durations are 89 ± 34 h. The velocity temporal decline in the trailing edge is separated into two parts by the velocity-bend: the first part, which is a steep temporal decline in the solar-wind velocity prior to the velocity-bend, has a duration of 31 ± 18 h and the second part, which is a shallow velocity temporal decline after the velocity-bend, has a duration of 57 ± 25 h. Typically, the second part of the velocity decline (velocity-bend to velocity termination) is about twice as long as the first part (initial velocity drop to velocity-bend), but there is a wide range of variation. In Figure 6 the observed total time duration of each trailing edge in Table 1 is plotted as a function of the predicted width from expression (3) (using expressions (1), (2a), and (2b)). As noted in the figure, the Pearson linear correlation coefficient between the observed width and the predicted width is $R_{corr} = +0.79$. The blue dashed line in Figure 6 denotes the locations of the observed width when they exactly match the predicted width.

The resulting collection of 54 high-speed-stream trailing edges contains 47 helmet-streamer trailing edges (being transitions from coronal-hole-origin plasma to helmet-streamer-origin plasma, having a single sector reversal in the slow wind) and contains six pseudostreamer trailing edges (being transitions from coronal-hole-origin plasma to pseudostreamer-origin plasma, without a sector reversal between the two high-speed streams); there is one trailing edge associated with a double sector reversal.

For each of the 54 high-speed-stream trailing edges the occurrence times of several characteristic features are recorded: the initial velocity drop, the velocity-bend, the midpoint of the drop in S_p, the midpoint of the strong rise in C^{6+}/C^{4+}, the midpoint of the strong rise in C^{6+}/C^{5+}, the midpoint of the strong rise in O^{7+}/O^{6+}, and the termination time of the declining velocity profile. These characteristic features were located from visual inspection of temporal plots, often with the aid of lines drawn upon the data plots. Some of these characteristic points will

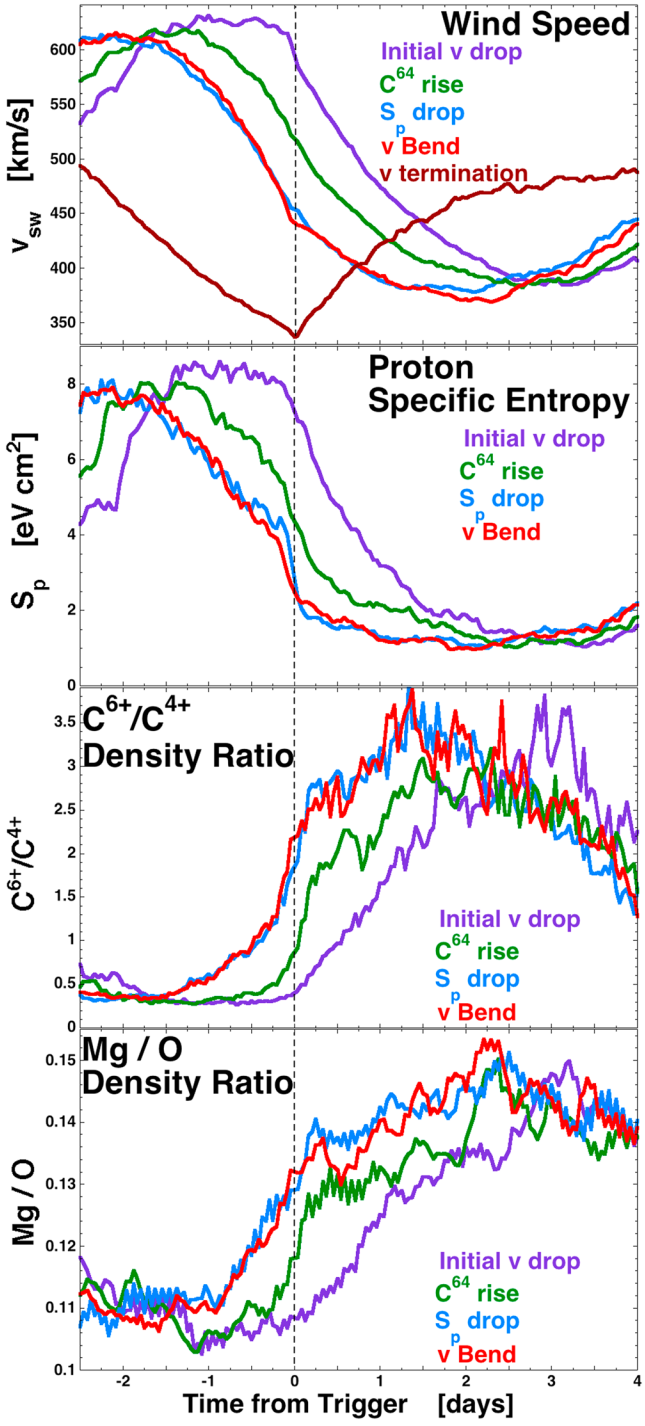

Figure 7. Superposed averages of candidate signatures for trailing-edge stream-interface identifiers are plotted vertically as functions of time with time organized according to various triggers. From top to bottom, (first panel) v_{sw} (OMNI), (second panel) the proton specific entropy (OMNI), (third panel) a carbon charge-state-density ratio ACE SWICS), and (fourth panel) the magnesium-to-oxygen elemental abundance ratio (ACE SWICS). The four colored curves are superposed averages triggered on the initial velocity drop (purple), the rise in C^{6+}/C^{4+} (green), the drop in S_p (blue), and the velocity-bend (red). In Figure 7 (first panel) an extra curve (brown) is triggered on the velocity terminations of the trailing-edge refractions.

be used to trigger superposed epoch averages of solar-wind measurements in the collection of high-speed-stream trailing edges. A goal is to discern which signature, if any, best describes the location of the trailing-edge stream interface.

With less stringent selection criteria, the authors also have a collection of 118 high-speed-stream trailing edges in the years 1998–2008. All of the findings that will be reported here for the 54 high-speed-stream trailing edges also hold for the larger collection of 118 trailing edges. Most of the 118 trailing edges that were rejected to make the list of 54 higher-quality trailing edges were rejected because the pressure and velocity perturbation of the CIR following the trailing edge is encroaching into the trailing-edge rarefaction; hence, the velocity of the trailing edge did not drop to low values and there was no reservoir of unperturbed slow wind at the end of the trailing-edge rarefaction.

4. Superposed Epoch Analysis: Identifying the Trailing-Edge Stream Interface

The stream interface is the boundary between coronal-hole-origin plasma and streamer-belt-origin plasma. Several methods have been used to identify the stream interface in CIRs (cf. section 1), including the reversal of the east-west flow deflection of the solar wind, the peak of the total pressure, a sudden increase in the proton specific entropy, the sudden change in the heavy-ion composition and in the FIP elemental abundance, or the peak in the plasma vorticity. Using the zero crossing of the east-west flow reversal is problematic since there are east-west offsets to the solar-wind flow that make it uncertain where to chose the single critical point in the broad reversal; this idea is much improved by the vorticity method [*Borovsky and Denton*, 2010c] which analyzes the solar-wind flows in a rotated local-Parker-spiral-oriented reference frame.

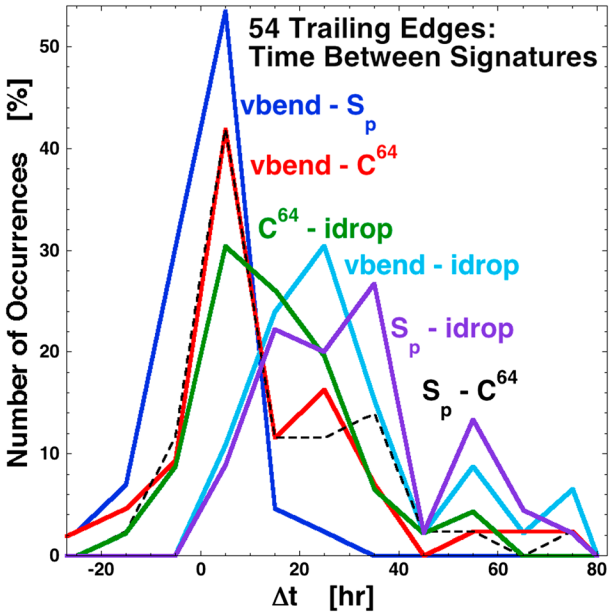

Figure 8. For the 54 trailing edges listed in Table 1, times are recorded for the initial velocity drop, the velocity-bend, the rise in C^{6+}/C^{4+}, and the drop in S_p. In the figure the time differences between these various time signatures are binned for the 54 trailing edges.

Three signatures will be explored to identify the stream interface in the high-speed-stream trailing edges: the sudden drop in the proton specific entropy S_p, the upward jump in the heavy-ion charge-state-density ratios (with C^{6+}/C^{4+} being the most robust signature), and the velocity-bend in the temporal velocity profile. (Algebraic schemes to categorize the solar wind into its constituent plasma types have been developed based on both O^{7+}/O^{6+} [*Zhao et al.*, 2009] and on S_p [*Xu and Borovsky*, 2015].) The preferred signature to locate the stream interface would be a peak in the vorticity, but in the individual high-speed-stream trailing edges isolated peaks in the vorticity are difficult to identify in the noise. Note that *Burton et al.* [1999] described factor-of-two changes in the FIP effect density ratio Mg/O as one of the signatures of the trailing-edge stream interface (a weak Mg/O signature can be seen in Figure 5). Examining high-speed-stream trailing edges at 1 AU, the authors found that it is, in general, not possible to select an unambiguous signature in the Mg/O 2-h resolution SWICS measurements owing to large oscillations in the Mg/O values. Other FIP-effect ratios such as Si/O and Fe/O were found to have similar behavior.

In Figures 7 (first panel) to 7 (third panel) superposed-epoch averages of the solar-wind velocity v_r (Figure 7, first panel), the proton specific entropy S_p (Figure 7, second panel), and the carbon charge-state-density ratio C^{6+}/C^{4+} (Figure 7, third panel) are plotted: in each panel the four colors are superposed averages triggered on the initial *v*-drop (purple), the upward jump in C^{6+}/C^{4+} (green), the drop in S_p (blue), and the velocity-bend (red). Figure 7 (fourth panel) plots the superposed average of the elemental density ratio Mg/O with the same color scheme. In Figure 7 (first panel) distinct features of the velocity profile are seen when the averaging is triggered on the initial *v*-drop (purple curve) and on the velocity-bend (red). Plotted in brown in Figure 7 (first panel) is the superposed average of the solar-wind velocity with the averaging triggered on the velocity termination times that mark the end of the trailing edges. Again, a sharp velocity feature is seen at $t = 0$ in this curve. In Figure 7 (second panel) the plot of S_p with the zero epoch being the S_p drop (blue curve) shows a sharp drop signature at $t = 0$ since all of the individual S_p drops are lined up in the averaging. Likewise in Figure 7 (third panel) the plot of C^{6+}/C^{4+} for the C^{6+}/C^{4+}-rise triggers (green curve) shows a somewhat sharper feature at $t = 0$: note that the superposed average of the C^{6+}/C^{4+} rise (green curve, Figure 7, third panel) is never as sharp as the superposed average of the S_p drop (blue curve, Figure 7, second panel) because, in general, the individual S_p drops are more sudden than the individual C^{6+}/C^{4+} rises. In all panels of Figure 7 the curves for the velocity-bend triggering and S_p-drop triggering are very similar: this is because the S_p-drop triggers and the velocity-bend triggers are close in time. Examining the time shifts of the four curves in the first panel, the statistical time separation of the four trigger types are seen, with the initial *v*-drop coming first, the C^{6+}/C^{4+} jump coming next, and the velocity-bend and S_p drop coming last. This trend is also seen in Figure 8 where the time intervals between the trigger times in the individual trailing edges are binned for the 54 trailing edges: the C^{6+}/C^{4+} trigger comes 15.5 h after the initial *v*-drop on average (green curve), the S_p-drop trigger time comes 30.5 h after the initial *v*-drop on average (purple curve), and the bend-*v* trigger comes 29.9 h after the initial *v*-drop on average (light blue curve). The C^{6+}/C^{4+} trigger is 14.0 h ahead of the bend-v trigger on average (red curve) and the S_p-drop is 0.5 h ahead of the velocity-bend on average (dark blue curve). (C^{6+}/C^{5+} and O^{7+}/O^{6+} triggers are at essentially the same times as the C^{6+}/C^{4+} triggers). The two signatures that are most likely to be used to determine the coronal-hole-plasma versus

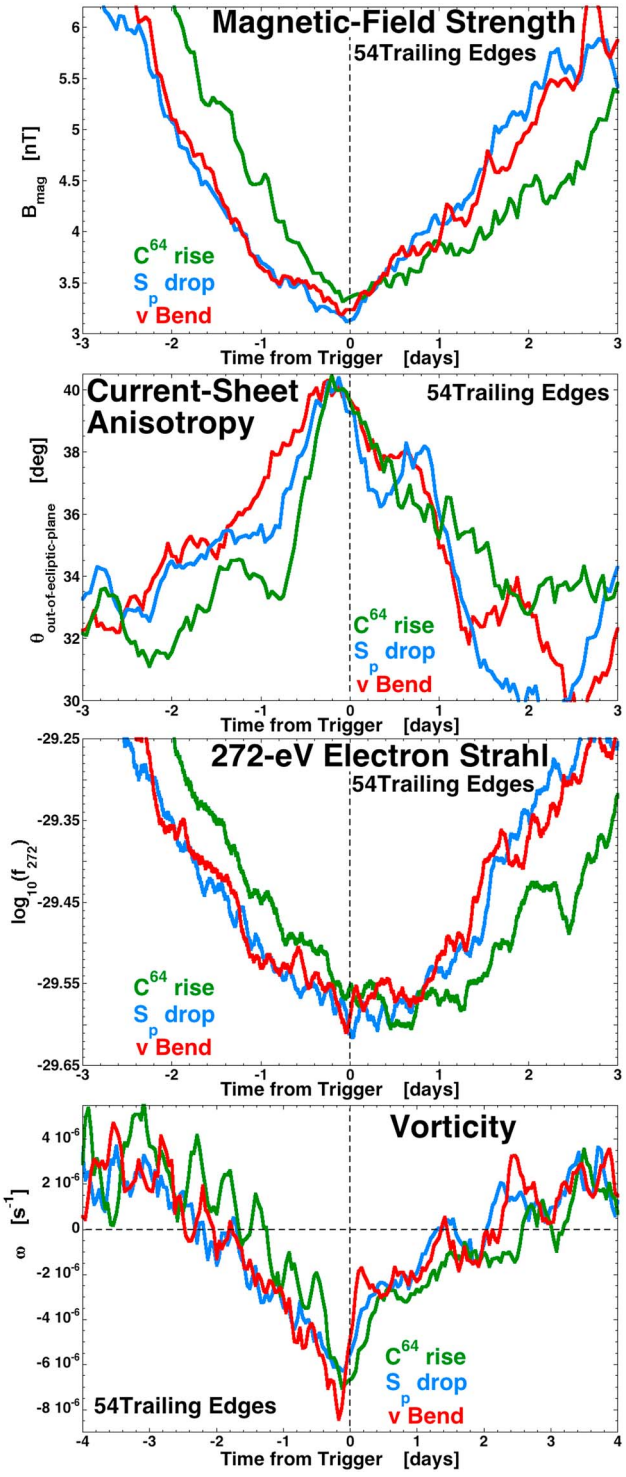

Figure 9. Superposed averages of four diagnostic parameters for the trailing-edge refractions are plotted as functions of time. From top to bottom, (first panel) the magnetic-field strength (OMNI), (second panel) the out-of-ecliptic angle of the current sheets (ACE Mag), (third panel) the intensity of the 272-eV electron strahl (ACE SWEPAM), and (fourth panel) the plasma vorticity (ACE SWEPAM). In each panel the green curve is a superposed-epoch average triggered on the C^{6+}/C^{4+} rise, the blue curve an average triggered on the S_p drop, and the red curve an average triggered on the velocity–bend.

streamer-belt-plasma boundary are the S_p drop and the C^{6+}/C^{4+} jump (dashed black curve in Figure 8): on average the C^{6+}/C^{4+} jump occurs 13.7 h prior to the S_p drop. *Zurbuchen et al.* [1999] also reported differences in the transition times in trailing edges, in particular, between the transitions of charge states (coronal) and of elemental abundances (photospheric). In Figure 7 (fourth panel) the superposed average of Mg/O is plotted for the four trigger signatures; here the superposed average of Mg/O behaves somewhat like the superposed average of C^{6+}/C^{4+} in Figure 7 (third panel), but noisier.

In Figure 9 superposed-epoch averages of four critical diagnostics of the trailing-edge rarefaction are plotted as functions of time triggered on the three stream-interface candidate signatures: those candidate signatures are the upward jump in C^{6+}/C^{4+}, the drop in S_p, and the velocity-bend. In Figure 9 (first panel) the superposed average of the magnetic-field strength B_{mag} in the 54 trailing edges is plotted. The decreased field strength within the trailing edge is caused by the rarefaction of the plasma. In Figure 9 (first panel) the S_p-drop triggering (blue curve) and the velocity-bend triggering (red curve) yield lower values of B_{mag} at the trigger point, implying that those signatures are locating the center of the rarefaction better than the C^{6+}/C^{4+} drop signature (green curve). For plasma that is neither compressed or rarefacted, two prior studies have found that the mean field strength in unperturbed coronal-hole plasma is 4.7 nT for a collection of flattop high-speed streams at 1 AU [cf. *Borovsky*, 2016, Table 4] and 6.2 nT for a collection of pseudostreamer streamer-belt plasma in *Xu and Borovsky* [2015]. Taking the mean of those two values, 5.5 nT is an estimate of what the field strength would be when not rarefacted. In Figure 9 (first panel) the field strength in the center of the rarefaction is 3.1 nT, so the estimated rarefaction factor is 5.5/3.1 = 1.8. In Figure 9 (second panel) the superposed average of the out-of-ecliptic angle $\theta_{\text{out-of-ecliptic}} = \text{invtan}(|n_n|/(n_r^2 + n_t^2)^{1/2})$ of current-sheet normals (see Appendix A) in the solar-wind plasma is plotted for

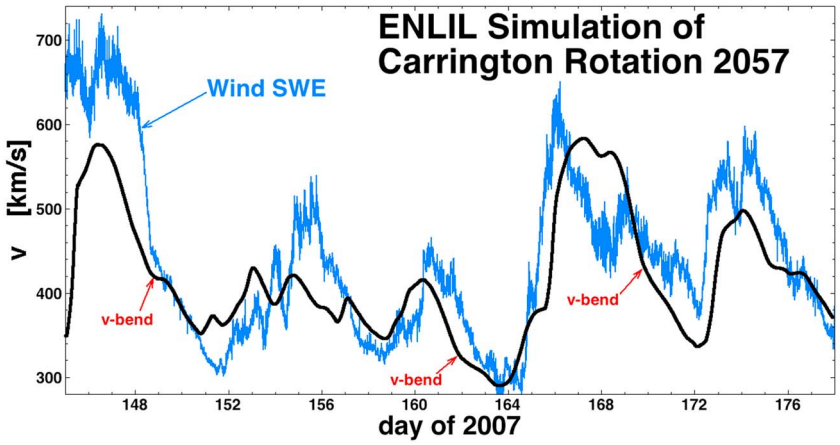

Figure 10. For an ENLIL 3-D MHD computer simulation of Carrington Rotation 2057 cataloged at the CCMC (run Lan_Jian_121311_SH_3), the solar–wind radial velocity at Earth is plotted in black. Also plotted in blue is the solar–wind speed measured by Wind SWE. The velocity–bends seen on the trailing edges in the ENLIL simulation are marked in red.

the collection of 54 trailing edges. The elevated value of $\theta_{\text{out-of-ecliptic}}$ inside the trailing edges is an indicator of solar-wind magnetic-structure stretching in the plasma owed to the rarefaction of the plasma. For a rarefaction by a factor of 1.8 (according to B_{mag}), the analysis of Appendix A predicts that the mean value of $\theta_{\text{out-of-ecliptic}}$ should increase from 32.7° to 44.3°: this is approximately the effect seen in Figure 9 (second panel). In Figure 9 (second panel) all three signatures (the upward jump in C^{6+}/C^{4+}, the drop in S_p, and the velocity-bend) do equally well (or equally poorly) at locating the maximum in the rarefaction as measured by the current-sheet anisotropy. In Figure 9 (third panel) the superposed-epoch average of the intensity of the 272-eV electron strahl is plotted for the three triggers. *Crooker et al*. [2010] suggested that the strahl intensity has a local maximum near the leading-edge stream interface because the strahl propagates away from the Sun there though a region that is maximally compressed and would have the solar-wind magnetic-field lines closest together to maintain the intensity of the strahl. If that is the case, we expect the strahl intensity to be a local minimum near the trailing-edge stream interface where the strahl propagates away from the Sun through a region that is maximally rarefacted. In Figure 9 (third panel) the strahl intensity is locally minimum near the zero epoch for the S_p-drop signature (blue curve) and for the velocity-bend signature (red curve), more so than for the C^{6+}/C^{4+}-rise signature (green curve). In Figure 9 (fourth panel) the superposed average of the *N*-component vorticity ω of the plasma flow is plotted for the 54 trailing edges. The velocity-bend signature seems to be best at locating the maximum of the negative vorticity, which is expected to occur at the stream interface.

In using Figure 9 to judge which of the three candidate signatures (the upward jump in C^{6+}/C^{4+}, the drop in S_p, or the velocity-bend) best denotes the location of the trailing-edge stream interface, there is no clear choice. Further, there are high-speed-stream trailing edges that have non-monotonic velocity profiles with multiple bends, multiple S_p drops, and/or multiple C^{6+}/C^{4+} jumps. (This is contrary to the impression of *Burton et al*. [1999], which was based on the examination of 18 recurrences of a single high-speed stream observed farther out (4.5–5 AU) and at higher latitudes (13–36°) where trailing-edge rarefactions might behave differently.) Weighing the evidence in Figure 9, the velocity-bend signature does as well or better than the other two signatures at locating the stream interface as diagnosed with B_{mag} as a measure of rarefaction, $\theta_{\text{out-of-ecliptic}}$ as a measure of rarefaction, the electron-strahl intensity as a measure of rarefaction, and ω as a measure of shear along the Parker spiral. The velocity-bend signature also has the advantage that it is robust and easily identified using plasma measurements. Often the velocity-bend can be located with a time accuracy of a minute or so.

Henceforth, the velocity-bend in the temporal velocity profile will be taken as the location of the stream interface in the trailing edge. This choice is validated by computer simulations.

ENLIL 3-D MHD simulations [*Odstrcil*, 2003] of the solar wind in the heliosphere produced by solar-wind emission from a rotating Sun display velocity breakpoints in the trailing edges of high-speed streams. In Figure 10

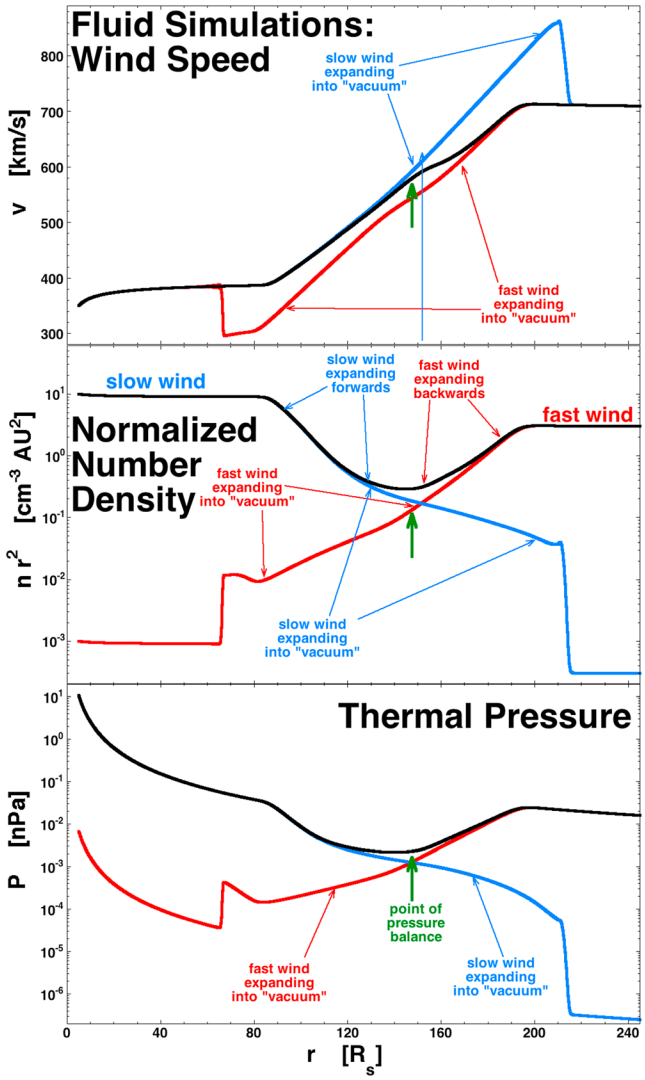

Figure 11. Using a one-dimensional (radial) fluid-simulation code in spherical geometry, three simulations are run and various quantities are plotted as a function of radius at the same time in each of the three simulations. The black curves are from a simulation with $n_{fast} = 3\ cm^{-3}$ and $n_{slow} = 10\ cm^{-3}$ (at 1 AU); the red curves are from a simulation with $n_{fast} = 3\ cm^{-3}$ and $n_{slow} = 0.001\ cm^{-3}$; the blue curves are from a simulation with $n_{fast} = 0.0003\ cm^{-3}$ and $n_{slow} = 10\ cm^{-3}$.

the solar-wind speed at Earth as predicted by ENLIL modeling is plotted in black as a function of time for Carrington rotation 2057 in the year 2007. The first high-speed-stream trailing edge in this plot is the example trailing edge of Figure 5. Noted in red in Figure 10 are distinct inflection points in the velocity profiles of three trailing edges. For reference, measurements of the solar-wind speed from Wind SWE are plotted in blue for the same time period.

To explore the origin of the velocity-bend in the trailing edges, one-dimensional fluid simulations in spherical geometry of the solar-wind advection and expansion out from the Sun are run. The fluid simulation code solves the equation of motion

$$\partial v_r/\partial t + v_r(\partial v_r/\partial r) = -(1/m_p n)\partial P/\partial r \quad (4)$$

on a one-dimensional grid in the radial direction to get updated values of $v_r(r)$ on the grid, then advects the plasma number density n, specific entropy S_p, and adiabatic index γ outward with the local velocity $v_r(r)$ onto a new spatial grid. The advection scheme distributes the content of each old grid point forward in time onto the new grid with a conservative interpolation scheme. The simulation then uses an adiabatic law $T = S_p\, n^{\gamma-1}$ to compute the temperature $T(r)$ on the grid from the values of $S_p(r)$, $\gamma(r)$, and $n(r)$ on the grid, then calculates the pressure $P(r) = nk_BT$ on the grid. With the updated values of the pressure on the grid, a new time step begins with the solution of expression (4) for an updated $v_r(r)$ on the grid. To simulate the observed nonadiabatic addition of heat to the solar wind as it cools expansively out from the Sun [cf. *Borovsky and Gary*, 2014], the effective adiabatic indices in Table 1 of *Freeman and Lopez* [1985] are used: in the simulations $\gamma = 1.2$ is taken for slow solar wind and $\gamma = 0.8$ is taken for fast solar wind. In Figure 11 a radial snapshot of a trailing edge evolving as it advects outward from the Sun is plotted as the black curves. In Figure 11 (top) the solar-wind velocity v_r is plotted in black as a function of distance from the Sun, in Figure 11 (middle) the normalized solar-wind number density nr^2 is plotted in black, and in Figure 11 (bottom) the plasma thermal pressure $P = nk_BT$ is plotted in black. The input parameters at the Sun in this simulation are chosen such that for steady outflow from the Sun $n_{slow} = 10\ cm^{-3}$ at 1 AU, $T_{slow} = 5$ eV at 1 AU, $n_{fast} = 3\ cm^{-3}$ at 1 AU, and $T_{fast} = 30$ eV at 1 AU. Earlier in the simulation the solar-wind speed at the inner boundary (5 R_s) rapidly changed from $v_{fast} = 700$ km/s to $v_{slow} = 350$ km/s. In the black curve in Figure 11 (top) note the inflection in the spatial profile of the flow velocity. To determine the origin of this velocity inflection, two other simulations are

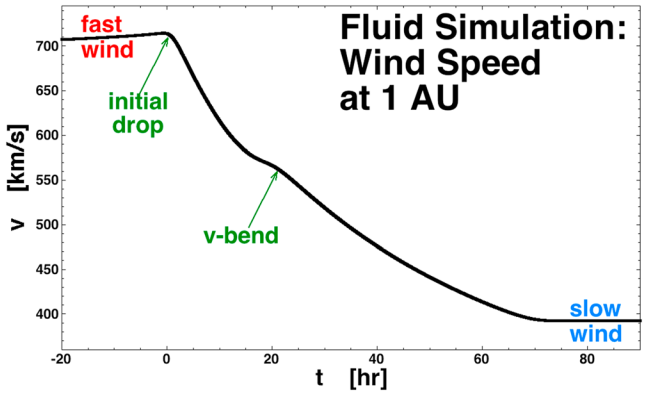

Figure 12. From the black-curve simulation of Figure 11, the solar-wind speed at 1 AU is plotted as a function of time. Time $t = 0$ is arbitrarily taken as the time when the initial velocity drop occurs at 1 AU.

run. In one simulation (blue curves in Figure 11), the number density of the fast wind is reduced by a factor of 10^4 to simulate the pressure expansion into "vacuum" of the slow wind outward off the front of the outward-advecting slow wind. In the other simulation (red curves in Figure 11), the number density of the slow wind is reduced by a factor of 10^4 to simulate the thermal expansion into "vacuum" of the fast wind sunward off the back of the outward advecting fast wind. In Figure 11 (top) one can see that the blue and red curves each follow the black curve until the vicinity of the black-curve inflection point is reached. This agreement indicates that those portions of the black curve represent unimpeded pressure expansion of the slow wind and the fast wind into the trailing-edge rarefaction. In Figure 11 (bottom) a green arrow denotes the point at which the thermal pressures of the blue slow-wind expansion into vacuum and the red fast-wind expansion into vacuum are close to equal. Here the slow-wind and fast-wind expansions will impede each other, forming an interface between slow-wind plasma and fast-wind plasma. In the black curve of Figure 11 (top) the expansions impeding each other produces a velocity that locally has a reduced slope. The green-arrow pressure-balance point where the pressure expansions of the fast-wind plasma and the slow-wind plasma collide is a good point to choose for the stream interface. The green arrow from Figure 11 (bottom) is reproduced in Figure 11 (top), showing the stream interface being very close to the location of the inflection point of the velocity spatial profile.

From the same black-curve simulation of Figure 11, the temporal profile of the solar-wind speed at 1 AU (215 R_s) is plotted in Figure 12 as the high-speed-stream trailing edge advects past the Earth. The initial drop and the velocity-bend in the temporal profile of the solar-wind velocity are noted with green labels.

The fluid simulations indicate that the inflection in the velocity profile is the point where the pressure expansions into the gap of the slow and fast plasmas meet: the slow plasma expanding forward (away from the Sun) and the fast plasma expanding backward (toward the Sun).

In Figure 13 the fraction of time that the *Xu and Borovsky* [2015] algebraic categorization scheme (which is based on the proton specific entropy S_p, the proton Alfven speed v_{Ap}, the proton temperature T_p, and the solar-wind speed v_{sw}) for the solar-wind plasma yields coronal-hole-origin plasma (red curves), streamer-belt-origin plasma (blue curves), sector-reversal-region plasma (green curves), and ejecta (purple curves) is plotted for the collection of 54 high-speed-stream trailing edges of Table 1. In Figure 13 (top) the time is organized about the initial velocity drops of the 54 trailing edges. Here it is seen that the initial velocity drop (vertical dashed line) corresponds to a time when the probability of coronal-hole-origin plasma is changing from 100% and the probability of streamer-belt-origin plasma is changing from 0%. In Figure 13 (middle) the data is organized according to the time of the velocity-bend in each trailing edge. In the categorization scheme the velocity-bend signature is occurring about where the occurrence probability of coronal-hole-origin plasma approaches 0% and where the combined probability of streamer-belt-origin and sector-reversal-region plasma approaches 100%. In Figure 13 (bottom) time is organized according to the velocity terminations of the 54 trailing edges. The velocity-termination signature (vertical dashed line) is occurring at a location where the categorization scheme says the probability of coronal-hole-origin plasma approaches 0% and the probability of seeing streamer-belt plasma is becoming a local minimum, and the probability of seeing sector-reversal-region plasma is becoming maximum. Unfortunately, there are not enough pseudostreamer trailing edges in the Table 1 collection to separately perform superposed epoch analysis for helmet-streamer versus pseudostreamers; pseudostreamers have no sector-reversal-region plasma in them.

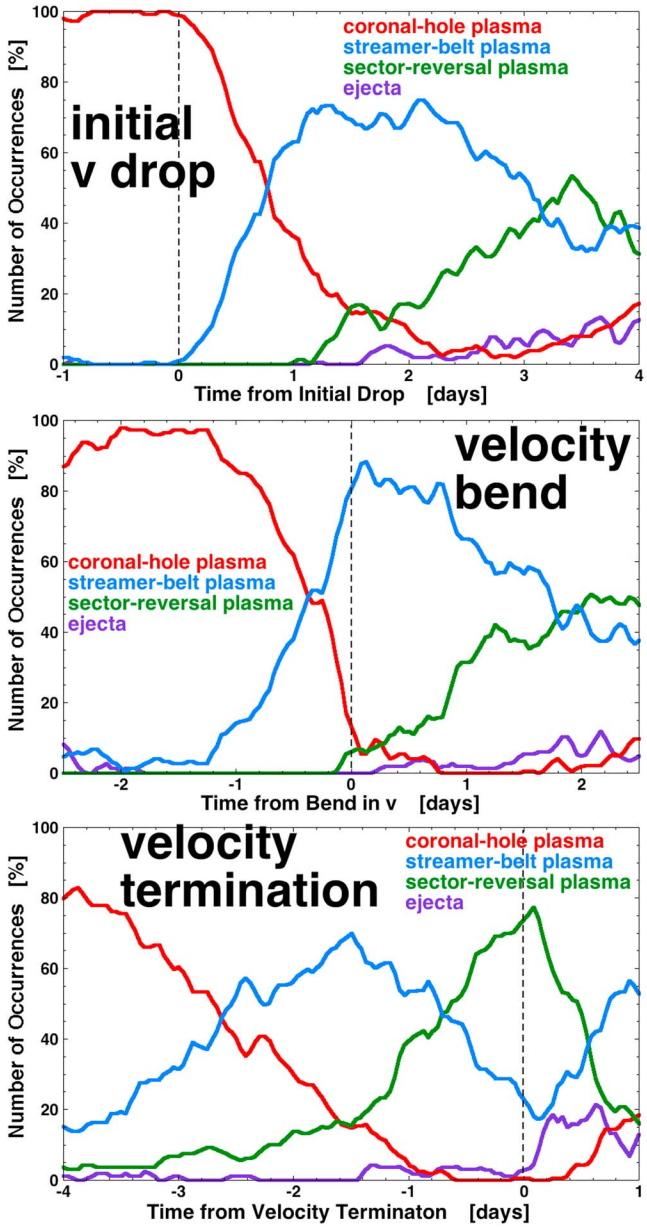

Figure 13. Using the *Xu and Borovsky* [2015] algebraic scheme to categorize the type of solar-wind plasma at 1 AU for the 54 trailing edges in Table 1, the percentage of time that each of the four types of plasmas appears is plotted as a function of time in four colors. (top) Time is organized about the initial velocity drop ($t = 0$) of the 54 trailing edges; (middle) time is organized about the velocity-bend ($t = 0$) of the 54 trailing edges; and (bottom) time is organized about the velocity termination ($t = 0$) of the 54 trailing edges.

5. The Properties of the Trailing Edges of High-Speed Streams

In this section the properties of the trailing edges will be studied using superposed-epoch analysis triggered on the velocity-bend signatures (taken as the trailing-edge stream interface) and on the termination times of the trailing edges. In section 6.1 the analysis will continue to be triggered on the initial velocity drop (taken as the onset of the trailing edge). This superposed-average study could have been performed by temporally stretching each time series for the individual trailing-edge rarefactions to line up simultaneously all of the velocity-bend signatures, all of the termination times, and all of the initial velocity drops. In some sense this would simplify the display of data, needing only one figure instead of three figures. But the choice was made to look at the superposed-epoch averaging individually for each type of trailing-edge critical signature.

Figure 14 examines the basic properties of high-speed-stream trailing edges in contrast to the examination of CIRs in Figure 3. Figure 14 (first panel) plots the superposed average of the solar-wind speed as a function of time, with the zero epoch of the 54 trailing edges being the velocity-bend in the temporal velocity profile of each trailing edge: the fast wind before and the slower wind after is seen, with the bend in the velocity profile readily apparent. In Figure 14 (second panel) the transverse velocity v_t has the pattern $-v_t$ first then $+v_t$, opposite to the temporal pattern of v_t in the CIR (see Figures 1 and 3, second panel). In Figure 14 (third panel) the plasma vorticity is negative in the trailing edge (cf. Figure 2), with a negative peak just prior to the velocity-bend. In Figure 14 (fourth panel), no sharp boundary in the plasma parameters of the solar wind are seen; however, there is an upward inflection of the superposed average of the proton number density at the time of the velocity-bend: this may be an indication of a transition from coronal-hole plasma to streamer-belt plasma with streamer-belt plasma having on average higher densities than coronal-hole plasma. In Figure 14 (fifth panel) the superposed average of the out-of-ecliptic angle of the current-sheet normals in the solar-wind plasma indicates a stretching (rarefaction) of the mesoscale magnetic-field structure of the solar-wind plasma in the trailing edge, with a peak just prior to the velocity-bend at $t = 0$. The superposed average of the intensity

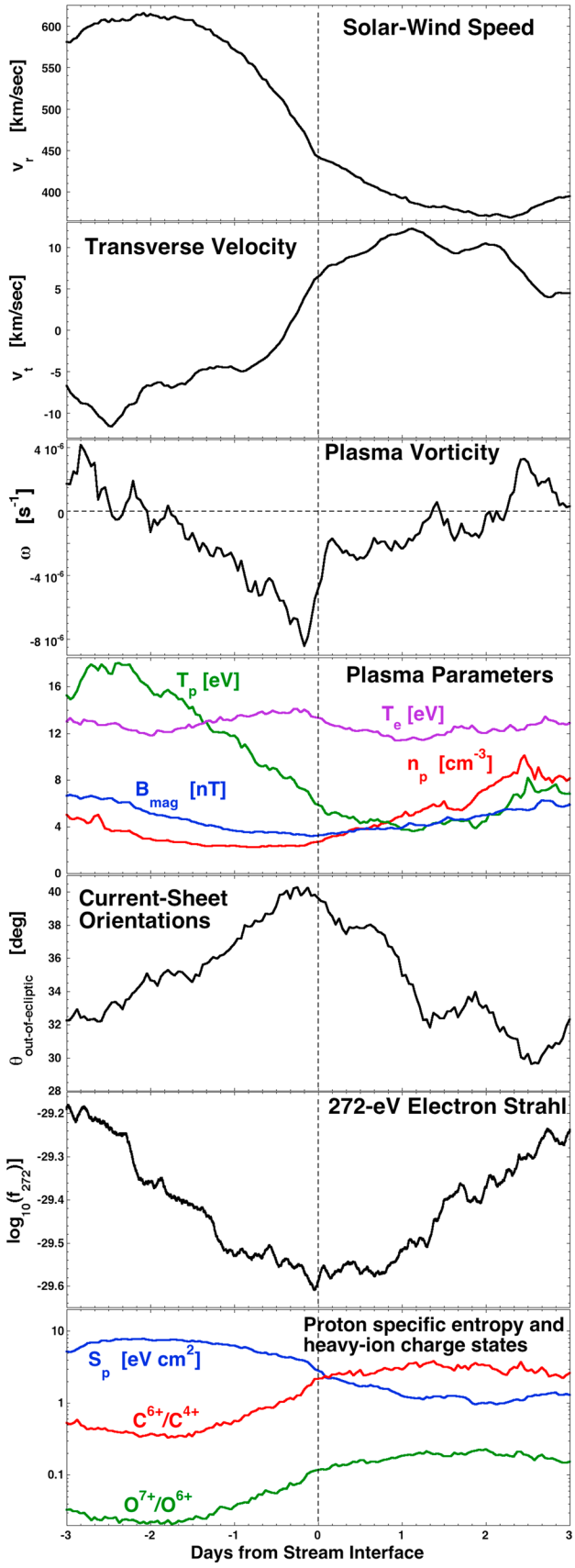

of the 272-eV electron strahl is plotted in Figure 14 (sixth panel). In this panel the strahl intensity is a minimum at the trailing-edge stream interface; this is expected in analogy to the *Crooker et al*. [2010] suggestion that the strahl is maximum where the compression is maximum; here the strahl is minimum where the rarefaction is maximum. In Figure 14 (seventh panel) the downward transition of the proton specific entropy S_p and the upward transitions of the heavy-ion charge-state density ratios are seen, with the S_p transition occurring after the heavy-ion transition in the superposed averages.

In Figure 15 some of the Alfvenic properties of the solar-wind plasma are explored via superposed-epoch averaging triggered on the velocity-bend of each trailing edge in the collection of 54. In the Figure 15 (first panel) the superposed average of the signed Alfvenicity [cf. *Borovsky and Denton*, 2010c]

$$A = s\,\delta v \cdot \delta B / |\delta v|\,|\delta B| \qquad (5)$$

is plotted, where the sign $s(t) = +1$ if the interplanetary magnetic field (IMF) is away from the Sun and $s(t) = -1$ if the IMF is toward the Sun. Positive A represents outward-sense Alfvenicity of the solar-wind $\underline{v}$ and $\underline{B}$ fluctuations and negative A represents inward-sense Alfvenicity. In Figure 15 (first panel) A is calculated on a 128-s timescale with ACE SWEPAM and ACE MAG. The superposed average of A is positive throughout the plot, with a decay

Figure 14. Superposed averages of measurements for the 54 trailing edges of Table 1 are plotted. The zero epoch (vertical dashed line) is the passage of the velocity-bend in each trailing edge. From top to bottom, (first panel) the solar-wind speed (OMNI), (second panel) the transverse velocity of the solar wind (OMNI), (third panel) the plasma vorticity (ACE SWEPAM), (fourth panel) the plasma number density (OMNI), proton temperature (OMNI), magnetic-field strength (OMNI), and electron temperature (Wind 3DP), (fifth panel) the out-of-ecliptic angles of the current-sheet normal vectors (ACE Mag), (sixth panel) intensity of the 272-eV electron strahl (ACE SWEPAM), and (seventh panel) the proton specific entropy (OMNI), the carbon charge-state-density ratio (ACE SWICS), and the oxygen charge-state ratio (ACE SWICS).

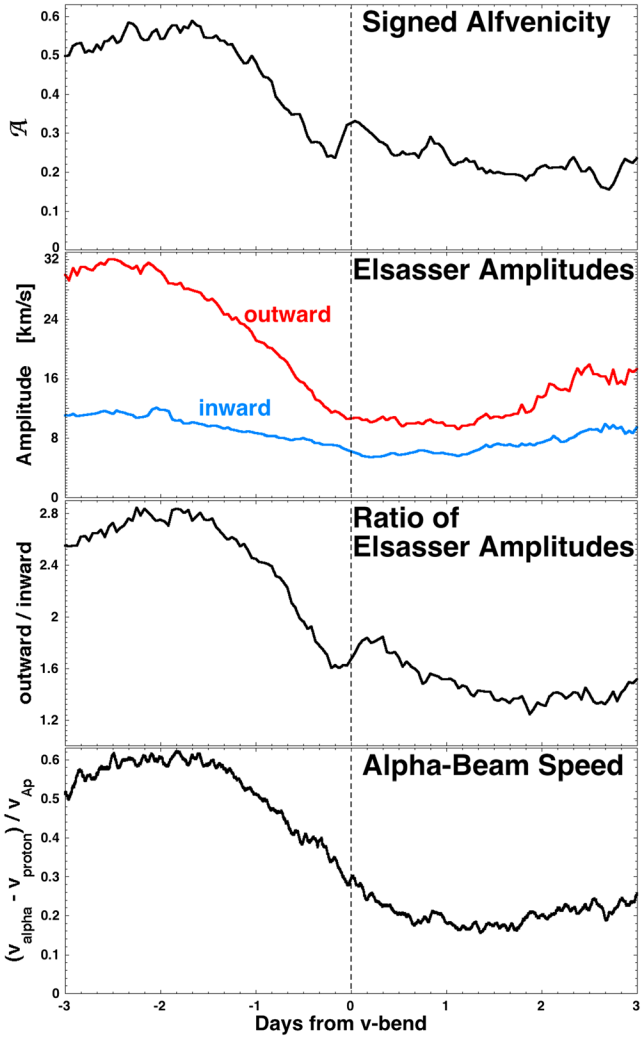

Figure 15. Triggered on the velocity-bend of the 54 trailing edges in Table 1, from top to bottom, (first panel) the superposed average of the signed Alfvenicity (expression (5)) (ACE SWEPAM and MAG), (second panel) the superposed averages of the amplitudes of the outward-sense (red) and inward-sense (blue) Elsasser fluctuations (ACE SWEPAM and MAG), (third panel) the superposed average of the outward-to-inward Elsasser amplitude, and (fourth panel) the superposed average of the velocity of the alpha beam relative to the proton velocity (normalized to the proton Alfven speed) (WIND SWE and Mag).

in the Alfvenicity across the trailing edge. At the velocity-bend ($t=0$) there is a non-monotonic inflection in the superposed average of A: the statistical significance of this inflection is difficult to gauge, as is the possible physical origin of the inflection. In Figure 15 (second panel) the superposed average of the amplitudes of the outward (red) and inward (blue) Elsasser fluctuations are plotted. The Elsasser amplitudes $\delta\underline{v} \pm \delta\underline{B}/(4\pi n m_i)^{1/2}$ [e.g., *Tu and Marsch*, 1995; *Bruno and Bavassano*, 1991] are calculated using ACE velocity, magnetic-field, and density measurements with 64-s time resolution and the amplitudes are plotted for the frequency range $f \geq 1\times10^{-3}$ Hz. The amplitude of outward Alfvenic fluctuations decays strongly prior to the v-drop (stream interface) at $t=0$ and ceases to decay thereafter. The amplitude of the inward Elassser fluctuations decays slightly in the trailing edge prior to the v-drop point at $t=0$ and then does not decay thereafter. In Figure 15 (third panel) the superposed average of the outward to inward Elsasser-variable amplitudes is plotted: the strong outward imbalance decays in the trailing edge prior to the v-drop point (stream interface) and does not decay appreciably afterward. Note the non-monotonic inflection in the superposed average of the ratio of Elsasser amplitudes in Figure 15 (third panel) looking very much like the inflection in the signed Alfvenicity in Figure 15 (first panel). In Figure 15 (fourth panel) the superposed average of the normalized alpha-particle beam speed in the solar wind (measured with Wind 3DP) $|\underline{v}_{alpha} - \underline{v}_{proton}|/v_{Ap}$ (normalized to the proton Alfven speed $v_{Ap} = B/(4\pi m_p n_p)^{1/2}$) is plotted. It is well known that the normalized beam speed is larger in the outward Alfvenic regions of the fast solar wind [e.g., *Marsch et al.*, 1982] and smaller in the less-Alfvenic slower wind [*Hirshberg et al.*, 1974; *Asbridge et al.*, 1976; *Marsch et al.*, 1982]. In Figure 15 (fourth panel) the decay of the normalized beam speed is seen in the trailing edge before the stream interface at $t=0$ and the decay is significantly less thereafter.

In the five panels of Figure 16 the plasma properties of the latter portions of trailing-edge rarefactions are investigated using superposed-epoch analysis triggered on the velocity terminations of the trailing edges in Table 1. In Figure 16 (first panel) the superposed average of the solar-wind speed is plotted: the long temporal decline of the velocity is clearly seen, with the velocity termination at $t=0$, which is the chosen trigger time. In the superposed average an increase in the solar-wind speed commencing at $t=0$ appears: not all of the individual events have such increases, but none have decreases so the superposed average shows a net increase. The Figure 16 (second panel) plots the superposed average of the transverse velocity v_t of the solar

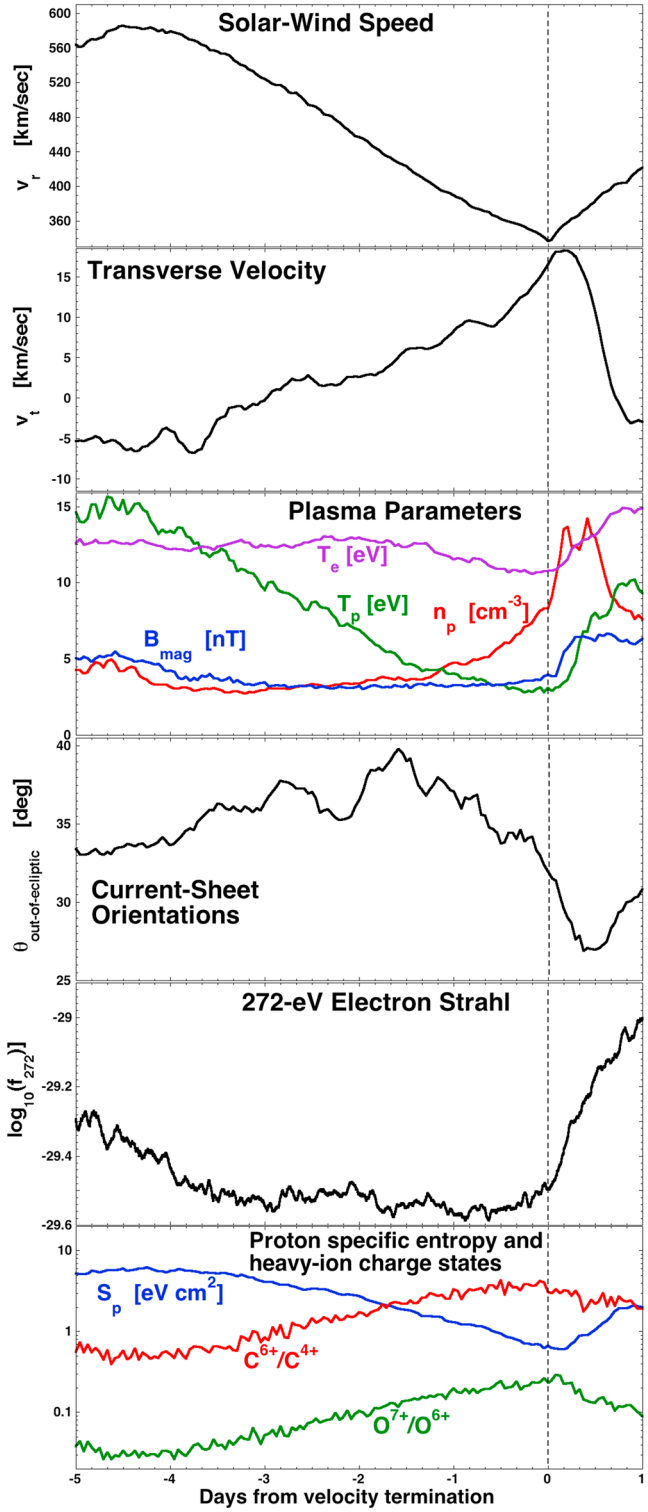

Figure 16. Superposed averages of measurements for the 54 trailing edges of Table 1 are plotted. The zero epoch (vertical dashed line) is the passage of the velocity termination in each trailing edge. From top to bottom, (first panel) the solar-wind speed (OMNI), (second panel) the transverse velocity of the solar wind (OMNI), (third panel) the plasma number density (OMNI), proton temperature (OMNI), magnetic-field strength (OMNI), and electron temperature (Wind 3DP), (fourth panel) the out-of-ecliptic angles of the current-sheet normal vectors (ACE MAG), (fifth panel) intensity of the 272-eV electron strahl (ACE SWEPAM), and (sixth panel) the proton specific entropy (OMNI), the carbon charge-state-density ratio (ACE SWICS), and the oxygen charge-state ratio (ACE SWICS).

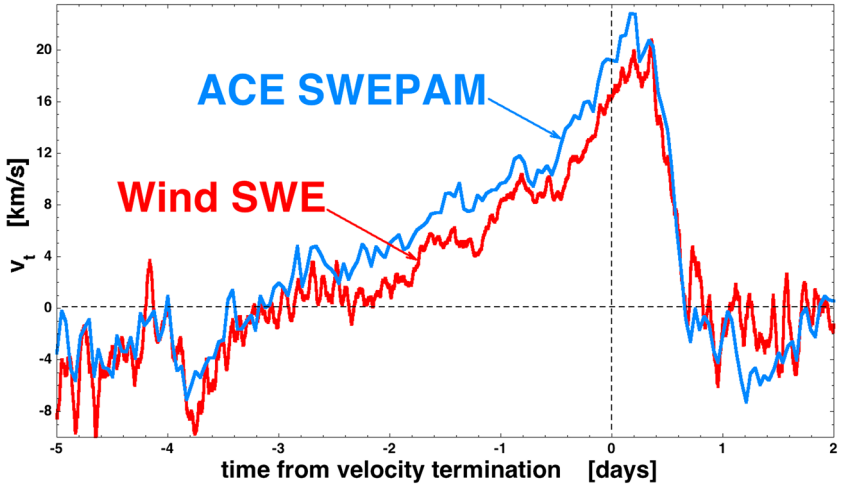

Figure 17. To check the veracity of the transverse velocity being maximum at the termination of the velocity decline, superposed averages are plotted separately for ACE electrostatic-analyzer measurements and Wind Faraday-cup measurements, both triggered on the velocity terminations of the 54 trailing edges in Table 1.

wind. The temporal pattern negative v_t then positive v_t of the trailing edge is seen in the days prior to the termination of the trailing edge at $t = 0$. Figure 16 (second panel) indicates that the positive v_t signature of the trailing edge peaks near the termination of the trailing edge: such a peaking of the transverse velocity at the end of the trailing-edge rarefaction is not seen in computer simulations [cf. *Pizzo*, 1991, Figure 12]. To verify the reality of this systematic positive v_t flow in the very slow solar wind, superposed-epoch averages of v_t are plotted in Figure 17 using data separately from the Wind SWE Faraday cup (red curve) and the ACE SWEPAM electrostatic analyzer (blue curve). The two instruments agree, indicating the reality of this systematic signal. One contributor to this positive transverse flow velocity v_t could be the onset of CIR events at the termination of some of the trailing-edge rarefactions. CIR onsets in the statistics also explains some of the increase in the solar-wind velocity after $t = 0$ in Figure 16 (first panel). When events that have velocity increases near to the velocity terminator are eliminated, the superposed average of v_t still shows this positive maximum at the time of velocity termination. The reduction of the superposed average of the out-of-ecliptic angle $\theta_{\text{out-of-ecliptic}}$ of the current-sheet normal vectors in Figure 16 (fourth panel) also indicates the presence of CIR compressions after time $t = 0$, although this reduction may be in part caused by the presence of aligned current sheets near the heliospheric sector boundaries [e.g., *Nakagawa et al.*, 1989; *Nakagawa*, 1993; *Crooker et al.*, 1993, 1996, 2001]. The increased (above 32°) value of $<\theta_{\text{out-of-ecliptic}}>$ before $t = 0$ indicates the broad rarefaction of the trailing edge. Figure 16 (third panel) plots the superposed average of some plasma properties: the magnetic-field strength (blue curve) indicates the broad rarefaction before $t = 0$. The reduced intensity of the electron strahl in Figure 16 (fifth panel) also supports this broad-rarefaction picture. Note in Figure 16 (third panel) the rise in the plasma number density (red curve) prior to $t = 0$; this rise may in part be caused by the increased likelihood that sector-reversal-region plasma is being encountered, with its enhanced density clumps. In Figure 16 (sixth panel) the superposed averages of the ion-charge-state density ratios C^{6+}/C^{4+} and O^{7+}/O^{6+} are plotted logarithmically along with the proton specific entropy S_p: note that C^{6+}/C^{4+} and O^{7+}/O^{6+} decline with time right up to the end of the trailing edge at $t = 0$ and that S_p increases with time right up to the end of the trailing edge. This supports the earlier reports [e.g., *Pagel et al.*, 2004; *Zurbuchen et al.*, 1999; *Simunac et al.*, 2010] of gradual transitions rather than abrupt transitions of the plasma properties.

In Figure 18 the properties of the fluctuations in the latter portions of high-speed-stream trailing edges are examined: again, superposed-epoch averaging triggered on the velocity terminations of the trailing edges is used. Figure 18 (first panel) plots the superposed average of the signed Alfvenicity (expression (5)); the fast-wind/slow-wind transition of the signed Alfvenicity from high values to low values across the long trailing edge prior to $t = 0$ is seen. In Figure 18 (second panel) the superposed averages of the outward-sense (red) and inward-sense (blue) Alfvenic fluctuations of $\underline{v}$ and $\underline{B}$ are plotted. The decay of the amplitude of outward fluctuations from faster solar wind to slower solar wind is seen across the trailing edge in the days prior to

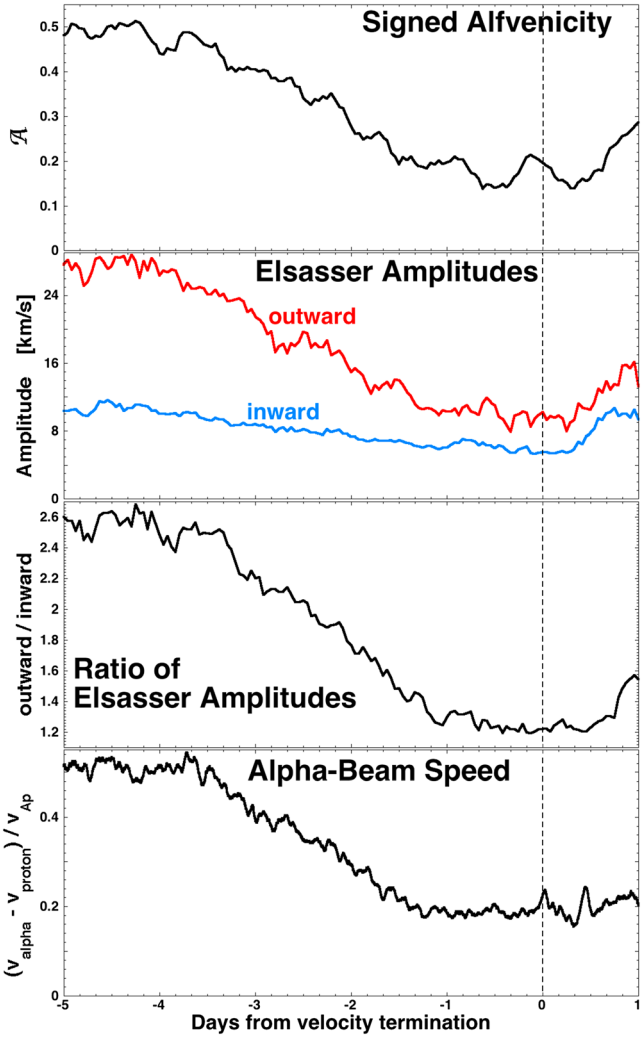

Figure 18. Triggered on the velocity termination of each of the 54 trailing edges in Table 1, from top to bottom, (first panel) the superposed average of the signed Alfvenicity (expression (5)) (ACE SWEPAM and MAG), (second panel) the superposed averages of the amplitudes of the outward-sense (red) and inward-sense (blue) Elsasser fluctuations (ACE SWEPAM and MAG), (third panel) the superposed average of the outward-to-inward Elsasser amplitude, and (fourth panel) the superposed average of the velocity of the alpha beam relative to the proton velocity (normalized to the proton Alfven speed) (WIND SWE and Mag).

$t = 0$. The superposed average of the ratio of the Elsasser amplitudes in Figure 18 (third panel) agrees with this, with the decay of the outward imbalance being caused by the decreasing amplitudes of the outward-sense Alfvenic fluctuations. Figure 18 (fourth panel) displays the decrease in the normalized speed of the alpha-particle beam in the solar-wind plasma: the temporal profile of the beam speed resembles the temporal profile of the outward imbalance in Elsasser amplitudes.

The early portions of the trailing edges are examined separately in section 6.1, where the onset of trailing edge is the focus of the discussion.

Figure 19 examines the robustness and reproducibility of the properties of high-speed-stream trailing edges. In Figure 19 (top) a high-speed-stream trailing edge (Trailing Edge #45 of Table 1, see also Figure 5) is viewed by three spacecraft at 1 AU with relatively close separations. In Figure 19 (top) Stereo A and Stereo B are separated by 10° of longitude (which is 0.75 days of solar rotation), with ACE and Wind (OMNI) in between the two. In Figure 19 (top) the velocity profile of the trailing is reproducible on the three spacecraft, with small-scale variations of v_r not reproduced from spacecraft to spacecraft. Note that the variation in v_r between the three spacecraft is greater in the high-speed stream than it is in the trailing-edge rarefaction (see also *Borovsky* [2016] for an examination of spatial structure in coronal-hole-origin solar-wind plasma). In Figure 19 (middle) Trailing Edge #47 of Table 1 is examined: here Stereo A and Stereo B are separated by 40.4° of longitude and by 5.4° of latitude, with OMNI between the two. 40.4° of longitude is 3.1 days of solar rotation. In this panel the velocity profile of the trailing-edge rarefaction is not very reproducible, and features like the initial velocity drop, the velocity-bend, and the velocity termination have quite different appearances in the three spacecraft cuts through the trailing edge. Note in Figure 19 (middle) that the structure of the high-speed stream preceding the trailing edge is very irreproducible between the three spacecraft views. In Figure 19 (bottom) Trailing Edge #53 of Table 1 is examined: here Stereo A and Stereo B are separated by 61.5° of longitude (4.6 days of solar rotation) and by 5.8° of latitude, with OMNI between the two. In this panel the velocity profile of the trailing-edge rarefaction is not very reproducible; i.e., the initial velocity drop looks different and the velocity-bend is sometimes difficult to identify. Again, in Figure 19 (bottom) the structure of the high-speed stream shows great variations from cut to cut by the three spacecraft. Figure 19 indicates that it is a matter of luck whether a particular trailing-edge rarefaction meets the criteria of section 3 to make it

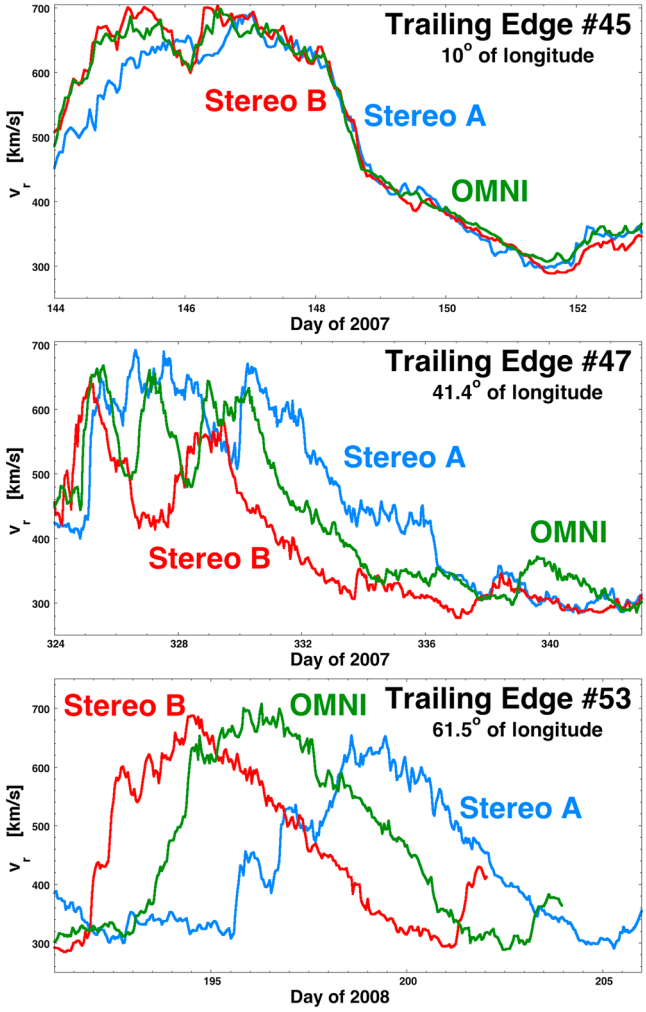

Figure 19. (top, middle, and bottom) For three trailing edges in the collection of Table 1, the velocity profiles of the trailing-edge rarefactions and the high-speed streams preceding them are examined with the Stereo A + B spacecraft at progressively increasing distances ahead and behind the Earth.

into the collection or whether it is deemed to be non-monotonic or irregular. Additionally, measurements of quantities like the temporal width of the trailing edge will have some variability.

6. Discussion

This section contains two discussions. The first (section 6.1) is a continuation of the examination of the properties of high-speed-stream trailing edges from section 5, organized under the question of whether or not the initial velocity drop is the initiation of the trailing-edge rarefaction. The second discussion (section 6.2) examines the leading and trailing edges of coronal holes on the Sun for clues about the origins of differences that are seen between the leading-edge stream interface and the trailing-edge stream interface seen in the solar wind at 1 AU.

6.1. Is the Initial Velocity Drop the Onset of the Trailing-Edge Rarefaction?

The initial velocity drop, assumed to be at the termination of the high-speed stream, has been taken to be the front of the rarefaction wave propagating antisunward into unperturbed coronal-hole-origin plasma, but that might be a misidentification.

Borovsky [2016] collected 66 intervals of solar-wind data at 1 AU that provided the best candidates for intervals of "unperturbed coronal-hole-origin plasma": the intervals selected were "flattop" high-speed streams, wherein the solar-wind velocity reaches a high level and then persists at that high level (with high-frequency noise) for a day or more. The temporal plot of v_r showed "flattops" on the high-speed streams. In making that collection, it was clear that the early portions of the flattops had to be eliminated from the data collection as being perturbed (compressed or rarefacted) because of elevated magnetic-field strengths indicating potential compression. Regardless of the seeming evidence of compression, the velocity was often constant in these eliminated early portions. When the solar-wind parameters were studied with superposed-epoch averaging triggered on the onsets of the collected flattop regions, solar-wind parameters were, in general, constant in the early portions of the flattops (after the elimination of the magnetic-field-perturbed portions). However, when the superposed averages were triggered on the termination of the flattop regions, the latter portions of the flattops showed systematically decreasing values of the proton number density and the magnetic-field strength, even though the velocity stayed constant. No systematic variation of the proton specific entropy or heavy-ion charge-state ratios was seen in the latter portions of the flattops. Except for the lack of a velocity variation, these observed trends could be indications of either (1) a rarefaction wave moving plasma into the trailing-edge gap or (2) super-radial expansion effects near the Sun at the edge of a coronal hole.

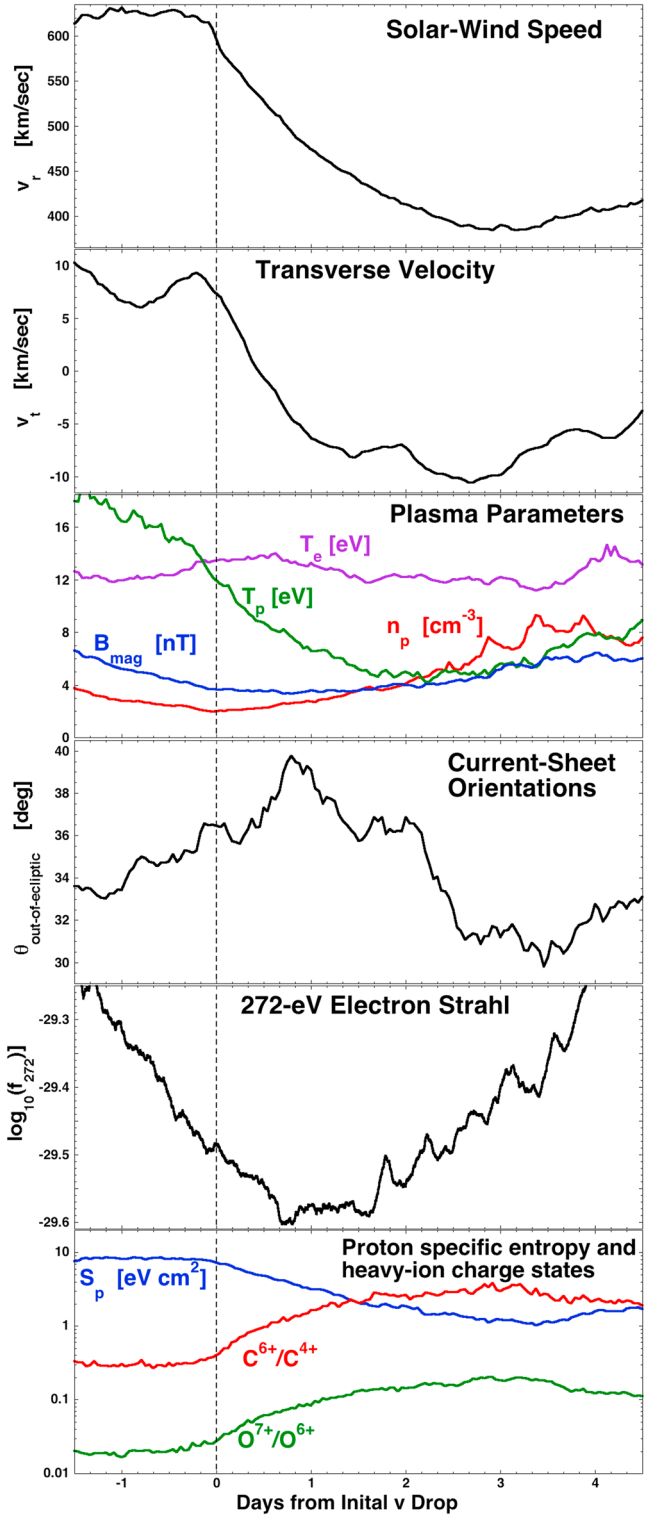

Figure 20. Superposed averages of measurements for the 54 trailing edges of Table 1 are plotted. The zero epoch (vertical dashed line) is the passage of the initial velocity drop in each trailing edge. From top to bottom, (first panel) the solar-wind speed (OMNI); (second panel) the transverse velocity of the solar wind (OMNI); (third panel) the plasma number density (OMNI), proton temperature (OMNI), magnetic-field strength (OMNI), and electron temperature (Wind 3DP); (fourth panel) the out-of-ecliptic angles of the current-sheet normal vectors (ACE MAG); (fifth panel) intensity of the 272-eV electron strahl (ACE SWEPAM); and (sixth panel) the proton specific entropy (OMNI), the carbon charge-state-density ratio (ACE SWICS), and the oxygen charge-state ratio (ACE SWICS).

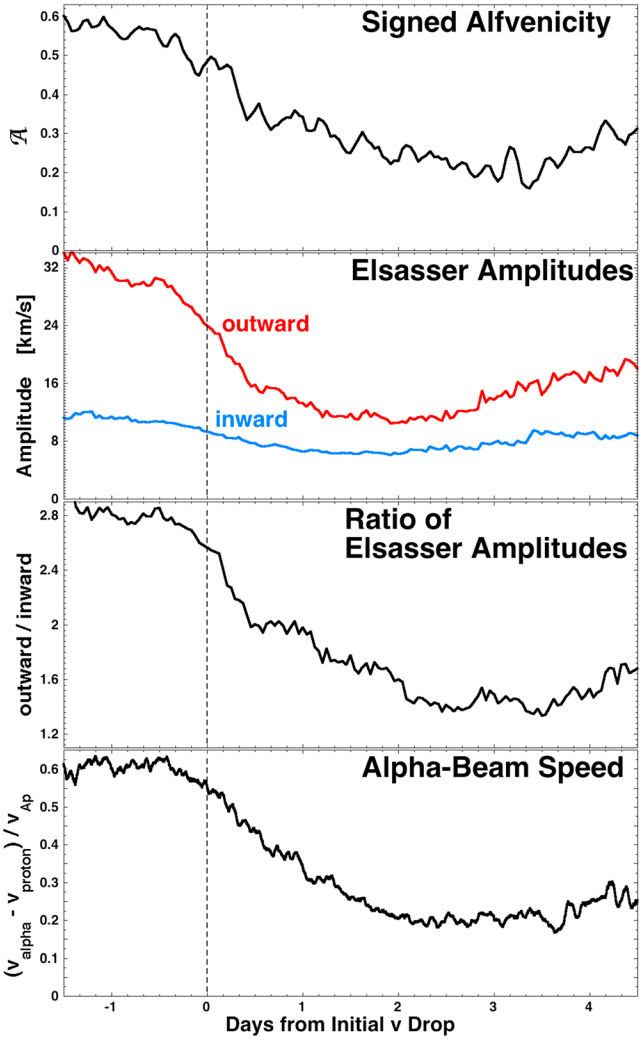

Figure 21. Triggered on the velocity-bend of the 54 trailing edges in Table 1, from top to bottom, (first panel) the superposed average of the signed Alfvenicity (expression (5)) (ACE SWEPAM and MAG), (second panel) the superposed averages of the amplitudes of the outward-sense (red) and inward-sense (blue) Elsasser fluctuations (ACE SWEPAM and MAG), (third panel) the superposed average of the outward-to-inward Elsasser amplitude, and (fourth panel) the superposed average of the velocity of the alpha beam relative to the proton velocity (normalized to the proton Alfven speed) (WIND SWE and Mag).

Figure 20 contains a layout of superposed averages triggered on the initial velocity drops (vertical dashed line) of the 54 trailing edges of the current study. Figure 20 (third panel) corroborates the temporal decline of n_p and B_{mag} in the latter portions of the high-speed streams reported in *Borovsky* [2016]. Figure 20 (second panel) indicates a strong positive transverse velocity v_t at and prior to the initial velocity drop, consistent with plasma pressure expansion into the trailing-edge rarefaction at these locations. In Figure 20 (fourth panel) the mean value of the current-sheet normal orientations $\theta_{out\text{-}of\text{-}ecliptic}$ is above 32.7° in the region before and at the initial velocity drop: according to the analysis of Appendix A (see figure therein) this would indicate that the solar-wind plasma in these regions has undergone some rarefaction. Edge-of-the-coronal-hole effects at the Sun might lead to magnetic structure that is unidirectionally stretched (Figure 20, fourth panel), but it would not lead to transverse flows at 1 AU (Figure 20, second panel). The decay of the superposed average of the electron-strahl intensity before the initial velocity drop in Figure 20 (sixth panel) also seems to supply evidence for a rarefaction prior to the initial velocity drop; however, *Borovsky* [2016] found that the intensity of the electron strahl systematically decays all the way across flattop high-speed streams (in individual cases and in the superposed averages). This total decay, of which the decay in Figure 20 (sixth panel) is part of, has not been explained.

Figure 21 examines some of the fluctuation properties of the trailing edge with superposed-epoch averaging triggered on the initial velocity drop. In Figure 21 (first panel) the superposed average of the signed Alfvenicity (expression (5)) is plotted: the Alfvenicity of the velocity- and magnetic-field fluctuations steadily declines from before the initial velocity drop until a few days afterward. In Figure 21 (second panel) the amplitude of the outward Alfvenic fluctuations decreases significantly from before the initial drop until a day or so afterward, while the superposed average of the inward amplitude declines only slightly. The outward imbalance of the fluctuations (Figure 21, third panel) has a decrease that begins prior to the initial velocity drop but the majority of the decrease is afterward. In Figure 21 (fourth panel) the superposed average of the normalized alpha-beam speed in the solar-wind plasma is plotted: the majority of the decrease in the beam speed comes after the initial velocity drop. Figure 21 finds that the changes in the properties of the fluctuations in the solar-wind plasma begin, for the most part, prior to the initial velocity drop. This is a further indication that the rarefaction wave front may be prior to the initial velocity drop.

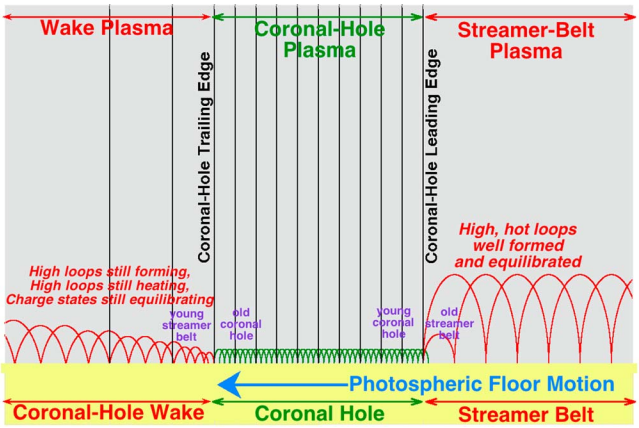

Figure 22. A sketch of the open flux of a coronal hole (with low-lying closed loops (green) on the coronal-hole floor) sandwiched between two regions of streamer belt (with higher closed loops (red)). In the reference frame of the coronal hole and its open flux, the photosphere (yellow) moves from right to left so that photosphere enters the coronal hole on the leading edge and exits the coronal hole on the trailing edge. It is hypothesized that the transition from open flux to closed flux at the trailing-edge boundary might have a temporal wake wherein it takes tens of hours to form high closed loops, to heat the high loops, and to reach charge-state equilibrium in the high loops.

If the rarefaction wave has propagated antisunward past the initial-velocity-drop point, then (1) the beginning of the trailing-edge rarefaction is at an as yet unidentified point before the initial velocity drop (by about a day) and (2) the initial velocity drop is a different feature in the trailing edge with an as yet unidentified origin.

6.2. The Leading-Edge and Trailing-Edge Stream Interfaces in the Solar Wind and the Leading and Trailing Edges of Coronal Holes

The leading-edge (CIR) stream interface at 1 AU has nearly simultaneous signatures (to within the 1-h time resolution of the heavy-ion measurements): a sudden increase of the proton specific entropy, a decrease of the heavy-ion charge-state level, and localized positive vorticity. The trailing-edge stream interface has much less simultaneity of its signatures, as summarized in Figure 8; in the trailing edge of the high-speed stream the different boundaries are typically separated in time by about 12 h.

Owing to the compression of the solar-wind plasma in the leading edge and the rarefaction of the solar-wind plasma in the trailing edge, one would expect that the sequence of signatures would be stretched out in time in the trailing edge in comparison with the leading edge. However, this compression-rarefaction time stretching is not enough to explain the timing of signatures in the trailing edge. Looking at the magnetic-field strength as a measure of compression and rarefaction (as in section 4), the superposed average of the magnetic-field strength in the CIR at the stream interface (Figure 3, fourth panel) yields $B_{mag} = 10.3$ nT at the compressed leading-edge stream interface and the superposed average of the magnetic-field strength in the trailing edge (Figure 14, fourth panel) yields $B_{mag} = 3.1$ nT at the rarefacted trailing-edge stream interface. Taking the ratio of these two field strengths gives a measure of the ratio of the compression to the rarefaction, which is a factor of $10.3/3.1 = 3.25$. Hence, time should be stretched by a factor of about 3.25 in the trailing edge relative to the leading edge. This factor of 3.25 is not sufficient to account for the large differences in the times of the various signatures in the trailing edge (Figure 8). There is also, in general, an absence of strong transition signatures of charge-state-density ratios and of the proton specific entropy in the trailing edges. The transitions in C^{6+}/C^{4+}, O^{7+}/O^{6+}, and S_p from coronal-hole-origin values to streamer-belt-origin values are dominated by long gradual transitions (cf. *Zurbuchen et al.* [1999], *Pagel et al.* [2004], or *Simunac et al.* [2010]) with jumps that are not particularly large nor particularly sudden (cf. Figure 5, third panel or Figures 7, second panel and 7, third panel).

One explanation of the differences in the timing of signatures in the leading versus trailing edges at 1 AU could be that solar-wind production differs at the leading and the trailing edges of coronal holes. In Figure 22 a coronal hole with its leading and trailing edges is sketched. The equatorial extensions of coronal holes tend to exhibit rigid rotation [e.g., *Timothy et al.*, 1975; *Adams*, 1976; *Hiremath and Hedge*, 2013] whereas the photosphere rotates differentially: in this mismatch coronal holes can lead the rotation of the photosphere. This produces a major difference between the leading and trailing edges of a coronal hole: in the reference frame of the coronal hole, at the westward leading edge the photosphere enters the floor of the coronal hole from the streamer belt and at the eastward trailing edge the photospheric floor of the coronal hole exits, the coronal hole moves into the streamer belt [cf. *Kahler*, 2010, Figure 1]. As noted in Figure 22, the "age" of the coronal-hole floor (with age being how long it has had open flux) increases going from the westward leading edge to the eastward trailing edge [cf. *Borovsky*, 2016]. Interchange reconnection is observed to

occur on the edges of coronal holes [*Baker et al*., 2007; *Subramanian et al*., 2010; *Krista et al*., 2011]; owing to this inflow-outflow difference the nature of the reconnection of open flux with closed loops may differ on these two edges [cf. *Fisk et al*., 1999a, 1999b; *Wang and Sheeley*, 2004], particularly concerning the properties of the plasma on the closed flux loops that feed plasma into the open flux tubes [*Kahler et al*., 2010]. Indeed, differences in westward-edge versus eastward-edge reconnection signatures have been reported [*Yang et al*., 2011], with more reconnection jetting observed on the leading (westward) edge than on the trailing (eastward) edge. The magnitudes of the differences between the trailing-edge and the leading-edge stream interfaces may depend on whether the high-speed-stream source is a rigidly rotating extension of a polar coronal hole versus a differentially rotating isolated coronal hole [*Zirker*, 1977; *Nash et al*., 1988; *Navarro-Peralta and Sanchez-Ibarra*, 1994].

As noted in Figure 22, the streamer-belt region adjacent to the westward leading edge is old, in the sense that its flux has been closed for a long time; high, well-developed arches should populate this region. On the contrary, the streamer-belt region adjacent to the eastward trailing edge is young in the sense that the photosphere there recently was an open-flux region; here the arches may not be so well developed, lacking high hot closed arches. As the open flux reconnects with the uppermost arches, high hot arches will feed plasma into the open flux at the leading edge, whereas lower and cooler arches will feed plasma into the open flux at the trailing edge. With loop height corresponding to the electron temperature and hence to the charge-state ratio [*Feldman et al*., 1999; *Gloeckler et al*., 2003], a gradual variation in the loop sizes on the Sun may map into a gradual transition of heavy-ion charge-state ratios in the solar wind.

To elaborate further, as sketched in Figure 22 there might be a wake-like diffuse boundary on the eastward trailing edge of the coronal hole making a slow temporal transition on the Sun from open-flux coronal-hole photosphere to closed-flux streamer-belt photosphere. As the photosphere goes into closed-flux configurations on the trailing edge of a coronal hole, there will be three important timescales: (1) the timescale for the formation of high closed flux loops, (2) the timescale for the electron heating of those high closed loops, and (3) the timescale for ionization to bring the heavy-ion populations into charge-state equilibrium with the electron temperature. (In this open-closed temporal wake at the trailing edge, there might also be straggling open flux in the temporally developing young streamer-belt region, as depicted in the sketch of Figure 22.) The time evolution of the coronal hole's trailing edge on the moving photosphere corresponds to a spatial evolution on the Sun, which maps to a time evolution in the solar wind for a spacecraft at 1 AU. Estimates of the three timescales in the photospheric flow from coronal-hole morphology to streamer-belt morphology are the following. First, the timescale for the formation of high closed loops in the newly created streamer belt may be obtained from flux-replacement (recycling) estimates: these estimates vary from 1.4 to 3 h [*Close et al*., 2004, 2005] to ~40 h [*Schrijver et al*., 1997; *Schrijver*, 2007]. Second, the timescale for heating the high hot (1–2 MK) closed loops is in the range of 1–6 h [*Sheeley*, 1980; *Kopp et al*., 1985; *Viall and Klimchuk*, 2011; *Reale*, 2014]. Third, the timescale for carbon and oxygen to reach charge-state equilibria by progressive ionization in the high hot (1–2 MK) loops is in the range of 10^4 s (for $n_e = 10^8\,\mathrm{cm}^{-3}$) to 10^6 s (for $n_e = 10^6\,\mathrm{cm}^{-3}$) (cf. Figure 1 of *Smith and Hughes* [2010] or Figure 3 of *Landi et al*. [2012]). Taking the geometric means of each of those three timescales yields a total time of 7.5 h + 2.4 h + 27 h = 37 h for the creation, heating, and equilibration of the high loops in the eastward trailing-edge wake of the coronal hole. Using the results of mappings of the Earth's solar-wind-origin foot point on the Sun with the Wang-Sheeley-Arge model [*Arge et al*., 2003] (data courtesy of Nick Arge, 2009) for the years 2004–2008, *Borovsky* [2016] observed the speed of the Earth's foot point across the floors of coronal holes to be 0.15 km/s to 1 km/s; the statistical value of 0.51 km/s was taken to be a general estimate of the speed of the Earth's solar-wind-origin foot point on the floors of coronal holes. The solar-wind-origin foot point speed is probably slower than 0.51 km/s near the edges of coronal holes owing to the super-radial expansion of the solar wind near the coronal-hole edges. Taking the speed of the foot point to be half of 0.51 km/s, the 37-h high-loop development time would correspond to a transition boundary thickness of 3.4×10^4 km on the photosphere, about one supergranule diameter [e.g., *Simon and Leighton*, 1964; *Hagenaar et al*., 1997; *Srikanth et al*., 2000], which is about 1/150 times the equatorial circumference of the Sun. In the absence of solar-wind rarefaction away from the Sun, the Earth would cross this transition in the solar wind in ~37 h, however, rarefaction in the trailing edge stretches the crossing time. With a rarefaction by about a factor of 1.8 (estimated in section 4 from the observed magnetic-field strength profiles for trailing edges), the 1 AU crossing time is almost doubled from ~37 h to ~66 h. This 66-h value is on the order of the thickness of the observed trailing edges at 1 AU and is on

the order of the timescales seen at 1 AU for the transition in the heavy-ion charge state of the solar wind from coronal-hole values to streamer-belt values (e.g., *Geiss et al.* [1995], *Zurbuchen et al.* [1999], and Figure 14).

It would be interesting to determine whether this wake-like high-loop transition can be imaged on the eastward trailing-edge boundaries of coronal-hole extensions relative to the sharper westward leading-edge boundaries. The estimated width of the trailing-edge transition is about 1 supergranule diameter.

Mapping the close-together solar-wind boundaries in the leading-edge stream interface to the leading-edge of a coronal hole and mapping the more diffuse solar-wind boundaries in the trailing-edge stream interface to the trailing edge of a coronal hole with Solar Probe Plus could be a huge aid for understanding the reconnection dynamics and boundary thicknesses on the two coronal-hole edges. Solar Probe Plus will not have ion-charge-state measurements to measure hot-loop plasma injected into open field lines, but perhaps electron-distribution-function measurements can be used in their place. Separate mappings for isolated coronal holes versus equatorward extensions would be even more powerful.

7. Summary

The findings of this study are as follows:

1. Fifty-four high-speed-stream trailing edges at 1 AU were collected in the years 1998–2008 and analyzed. For each trailing edge, five signatures were recorded: the initial velocity drop at the end of the high-speed stream, the upward jump in the C^{6+}/C^{4+} charge-state-density ratio, the upward jump in the O^{7+}/O^{6+} charge-state ratio, the downward jump of the proton specific entropy S_p, and the bend in the declining velocity temporal profile.
2. The observed temporal widths of the trailing-edge rarefactions are described by simple ballistic arguments. The mean value and standard deviation of the temporal durations of the trailing edges in the collection is 89 ± 34 h.
3. The velocity-bend separates the trailing-edge rarefaction into two parts: the first part (prior to the velocity-bend) is typically about half as long in time as the second part (after the velocity-bend).
4. A measure of plasma compression and rarefaction was developed that uses the measured orientations of current sheets in the solar-wind plasma. The current-sheet orientations change when the magnetic structure of the solar-wind plasma is flattened in a compression or stretched in a rarefaction.
5. The leading-edge and trailing-edge stream interfaces are not symmetric; specifically, signatures of the leading-edge (CIR) stream interface occur approximately simultaneously whereas stream interface signatures in the trailing-edge rarefaction are temporally separated. Compression versus rarefaction is not enough to account for the leading-edge versus trailing-edge timing differences.
6. The velocity-bend was taken as the best signature to locate the trailing-edge stream interface. The velocity-bend provides the clearest signature of the maximum of the trailing-edge rarefaction as gauged by the magnetic-field strength, the orientation of the plasma current sheets, and the intensity of the electron strahl and the velocity-bend is closest to the maximum of the negative vorticity in the trailing edge.
7. One-dimensional computer simulations indicate that the velocity-bend is the collision point of the pressure-driven expansions of the slow streamer-belt-origin wind and the fast coronal-hole-origin wind in the trailing-edge rarefaction.
8. The downward jump of the proton specific entropy S_p in the trailing edge usually occurs near the velocity-bend.
9. The upward jumps in C^{6+}/C^{4+} and O^{7+}/O^{6+} tend to occur prior to the velocity-bend and prior to the downward jump of S_p.
10. The outward imbalance of the Alfvenic fluctuations has a high value in the high-speed streams: the value decays strongly from the high-speed stream to then velocity-bend and the decay rate is slow thereafter. The variation in the outward imbalance is owed to a variation in the amplitude of outward fluctuations.
11. At what appears to be the beginning of the trailing-edge rarefaction, there is an initial velocity drop that terminates the high-speed stream. However, although the velocity does not show a decrease, there are other signatures before the initial velocity drop (magnetic-field strength, Alfvenicity, current-sheet orientations) that imply that the trailing-edge rarefaction begins prior to this initial velocity drop.
12. It was speculated that the origins of the observed differences of leading-edge stream interfaces and trailing-edge stream interfaces at 1 AU might originate from differences in the leading and trailing

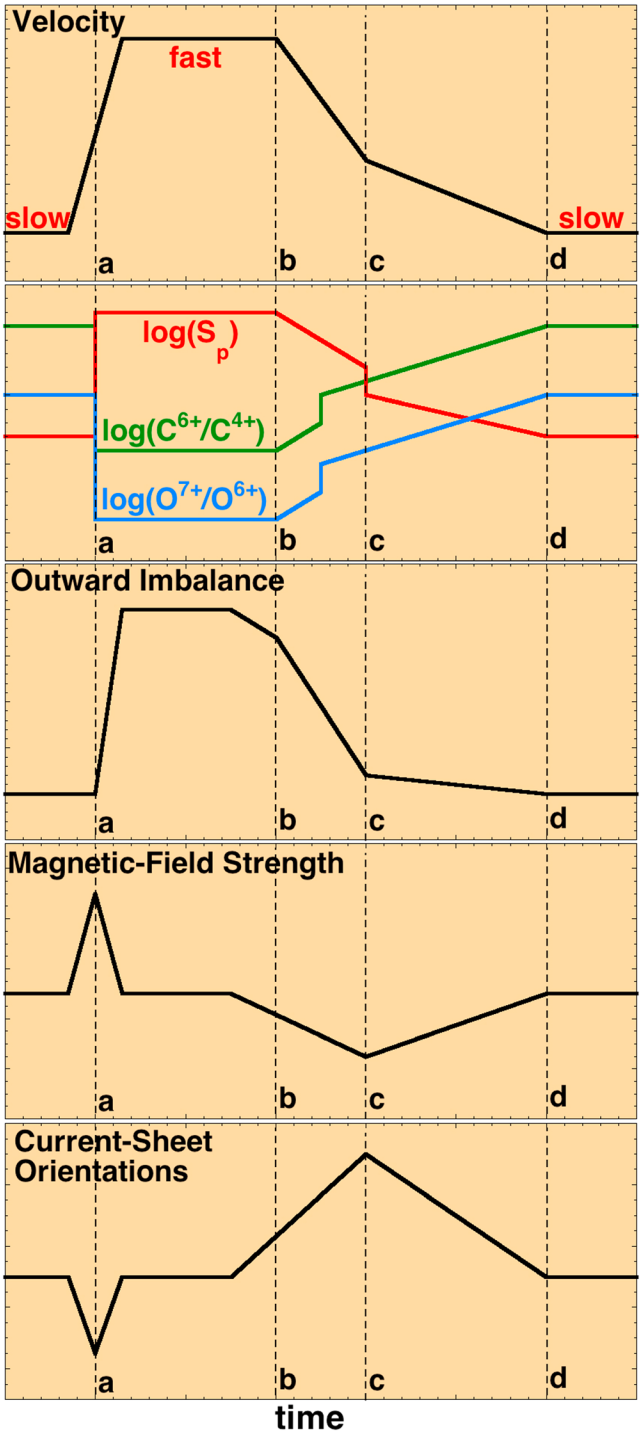

Figure 23. (first to fifth panels) A working sketch to organize the timing of the signatures in a high-speed stream, its leading-edge CIR compression, and its trailing-edge rarefaction. The four vertical dashed lines are a = leading-edge (CIR) stream interface, b = initial velocity drop, c = velocity-bend (trailing-edge stream interface), d = velocity termination of trailing edge.

edges of coronal holes on the Sun. These differences on the Sun might be owed to the rigid rotation of coronal holes versus the differential rotation of the photosphere and might involve the growth time, the heating time, and the charge-state-equilibration time for high closed loops in the eastern trailing-edge wake of the coronal hole.

A sketch organizing the chronology at 1 AU of the major signatures in the high-speed-stream trailing edge appears in the five panels of Figure 23. The four vertical dashed lines in the panels are the occurrence times of (a) the leading-edge (CIR) stream interface, (b) the initial velocity drop, (c) the velocity-bend in the trailing-edge rarefaction, and (d) the termination of the trailing edge. The initial velocity drop (b) is nominally taken as the start of the trailing-edge rarefaction, but there is evidence indicating that the rarefaction might start sooner. The velocity-bend (c) is taken as the location of the trailing-edge stream interface. In Figure 23 (first panel) the solar-wind velocity is sketched. Regions identified as slow wind and as fast wind are labeled, with the fast-wind interval being the high-speed stream. The solar-wind velocity rises across the CIR, taking about 1 day to go from low speeds to high speeds. The locations of the initial velocity drop (b) and the velocity-bend (c) are both obtained from an examination of the temporal profile of the solar-wind velocity. The termination (d) of the trailing edge is taken to be the point where the solar-wind velocity becomes constant or begins to rise after the long-duration decline in speed. In Figure 23 (second panel) the heavy-ion charge-state-density ratios C^{6+}/C^{4+} and O^{7+}/O^{6+} are sketched along with the proton specific entropy S_p. All three quantities change rapidly at the CIR stream interface (a), with C^{6+}/C^{4+} and O^{7+}/O^{6+} making the downward transition from streamer-belt-origin plasma to coronal-hole-origin plasma and S_p

making the upward transition from streamer-belt-origin to coronal-hole-origin plasma. C^{6+}/C^{4+}, O^{7+}/O^{6+}, and S_p begin to make the opposite transitions at the initial velocity drop (b) and complete their transitions at the terminator (d). The tendency in these long transitions is that C^{6+}/C^{4+} and O^{7+}/O^{6+} will exhibit a sudden jump upward in that long transition before S_p exhibits a sudden downward jump. (The upward jump in C^{6+}/C^{4+} during the long transition can be seen in the green curve in Figure 7 (third panel) at the time of the zero epoch; note that the upward jump in C^{6+}/C^{4+} is not as sudden as the drop in S_p, which is the blue curve in Figure 7 (second panel).) The C^{6+}/C^{4+} and O^{7+}/O^{6+} sudden upward jumps occur between the initial velocity drop (b) and the velocity-bend (c); the sudden downward jump of S_p occurs near the time of the velocity-bend (c). In Figure 23 (third panel) the outward Alfvenic imbalance of the solar-wind fluctuations is sketched. The transition from weakly Alfvenic slow wind to highly Alfvenic fast wind commences at the CIR stream interface (a) and ends at the end of the CIR. The Alfvenic imbalance of the high-speed stream begins to decline before the initial velocity drop (b), and the rate of decline becomes more rapid after the initial velocity drop. The decline in outward imbalance is almost complete at the time of the velocity-bend (c) and it declines very slowly thereafter. In Figure 23 (fourth panel) the magnetic-field strength of the solar wind is sketched. The field strength undergoes a compression in the CIR that peaks at the CIR stream interface (a). The field strength is constant through some of the high-speed stream, but it begins to decline prior to the time of the initial velocity drop (b). The magnetic-field strength is a minimum at the velocity-bend (c) and increases slowly thereafter. Prior to the initial velocity drop (b), the onset of the temporal decrease of the magnetic-field strength, the onset of the outward Alfvenic imbalance, and other signatures (e.g., the current-sheet orientation, the transverse flow velocity, and the outward Alfvenicity) provide indications that the trailing-edge rarefaction may begin prior to the initial velocity drop. In Figure 23 (fifth panel) the mean value of the out-of-ecliptic angle $\theta_{\text{out-of-ecliptic}}$ of the current-sheet normal vectors in the solar-wind plasma is sketched. The angle being reduced in the CIR indicates compression of the solar-wind plasma, and the angle being increased in the trailing edge indicates rarefaction of the solar-wind plasma; the compression peaks at the CIR stream interface (a) and the rarefaction peaks at the trailing-edge stream interface (c).

Appendix A: Compression and Rarefaction of Magnetic Structure

The microscale magnetic structure of the solar wind can be described as magnetic flux tubes bounded by strong current sheets [*McCracken and Ness*, 1966; *Mariani et al*., 1983; *Bruno et al*., 2001, 2004; *Borovsky*, 2008; *D'Amicis et al*., 2012; *Bruno and Carbone*, 2013]. The origin of the strong current sheets (and the flux tubes) may be the Sun [*Borovsky*, 2008; *Neugebauer and Giacalone*, 2010; *Owens et al*., 2011] or the flux tubes and current sheets may be generated locally in the solar-wind plasma [*Vasquez and Hollweg*, 1999; *Tsurutani and Ho*, 1999; *Greco et al*., 2009; *Zhdankin et al*., 2012]. The flux tubes are aligned approximately along the Parker spiral [*Borovsky*, 2010] and at 1 AU the normal vectors to the current sheets bounding the flux tubes are approximately perpendicular to the Parker spiral [cf. *Borovsky*, 2008, Figure 8] and quasi-isotropic about the Parker spiral [cf. *Borovsky*, 2008, Figure 7]. The quasi-isotropy of the current-sheet orientations implies that at 1 AU the flux-tube cross sections are approximately round. (More accurately, the flux-tube cross sections are in the form of a Voronoi pattern with an approximately equal aspect ratio in the two directions normal to the flux-tube axes (cf. Figure 1b of *Borovsky* [2008] or Figure 25 of *Borovsky* [2016].) An example round flux tube is depicted in Figure A1 (top). A series of spacecraft trajectories that pierce through the round (cylindrical) flux tube are depicted as the blue arrows; where each trajectory crosses through the front boundary of the flux tube, the normal vector to the current sheet is denoted with a red vector. The orientation of the current-sheet normal vectors has a range of values from vectors parallel to the ecliptic plane (for a spacecraft piercing the center of the tube) to vectors strongly out of the ecliptic plane (for piercings far from the center of the tube).

Unidirectional compression will squash (flatten) the magnetic structure of the solar wind in the direction of the compression while leaving the other direction unchanged: such a CIR-like compression (by a 2-to-1 factor) is depicted in Figure A1 (middle). Again, a series of spacecraft trajectories is depicted as the blue arrows in the sketch and the normal vectors to the current sheet at the points of piercing are again denoted with red vectors. Note that for the compressed flux tube the normal vectors tend to be focused toward the ecliptic plane relative to the normal vectors for the uncompressed round flux tube.

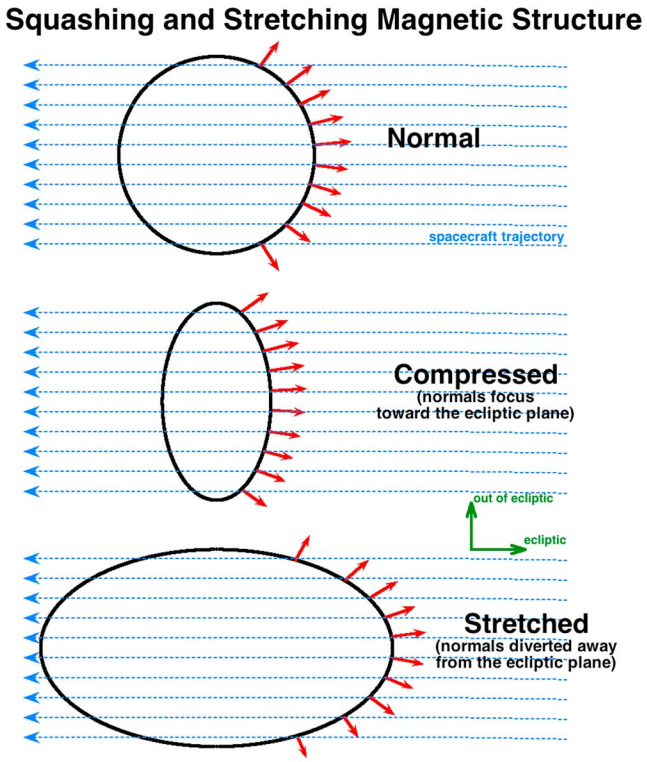

Figure A1. For (top) a round flux tube, (middle) a compressed flux tube, and (bottom) a rarefacted flux tube, red arrows mark the orientations of the normal vectors to the current sheet that bounds the flux tube. The coordinate system is indicated in green.

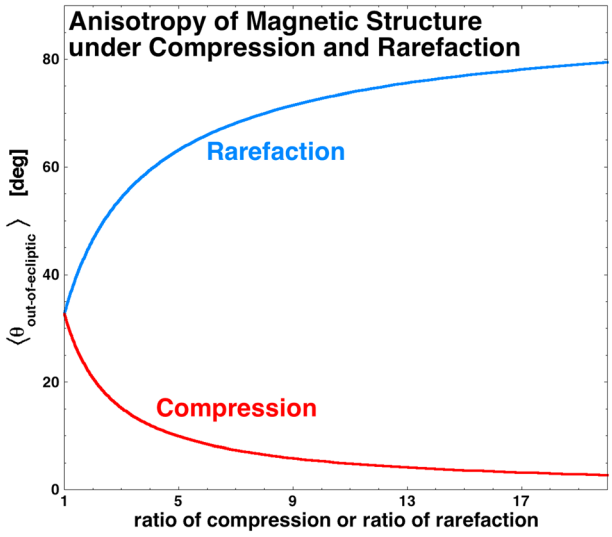

Figure A2. For flux tubes with elliptical cross sections, the mean value of the out-of-ecliptic angle of the current-sheet normal vectors of the flux-tube walls are numerically calculated and plotted as a function of the amount of compression (red) of the flux tubes or rarefaction (blue) of the flux tubes.

Unidirectional expansion (rarefaction) will stretch the magnetic structure of the solar wind in the direction of the expansion: such a trailing-edge-like rarefaction (by a factor of 2 to 1) is depicted in Figure A1 (bottom). And again, a series of spacecraft trajectories is depicted as the blue arrows and the normal vectors to the current sheet at the points of piercing are again denoted with red vectors. Note that for the rarefacted flux tube the normal vectors tend to be turned away from the ecliptic plane relative to the normal vectors for the uncompressed round flux tube.

For ellipsoidal round, compressed, and rarefacted flux tubes, the distribution of current-sheet normal vectors that a spacecraft would measure can be calculated numerically. For each normal vector (n_r,n_t,n_n), the out-of-ecliptic angle $\theta_{\text{out-of-ecliptic}} = \text{invtan}(|n_n|/(n_r^2 + n_t^2)^{1/2})$ can be calculated. The mean angle of the normal vector out of the ecliptic plane for such numerically calculated distributions is plotted in Figure A2 as a function of the degree of compression or rarefaction: the red curve is the mean angle for compressions and the blue curve is the mean angle for rarefactions. As seen in Figure A2, compression of the flux tubes reduces the mean angle (turns the normal vectors toward the ecliptic plane) and rarefaction of the flux tubes increases the mean angle (turns the normal vectors away from the ecliptic plane), as depicted in Figure A1.

Note that locally, the axes of the flux tubes of the solar wind are not perfectly aligned with the Parker spiral, rather there is a scatter of orientations about the Parker-spiral direction [cf. *Borovsky*, 2010, Figure 18]. At 1 AU the spread in flux-tube orientations out of the ecliptic plane had an average half angle of 38° for all solar wind in the years 1998–2006. The tilting of flux tubes out of the ecliptic plane will reduce high values of the out-of-ecliptic angles $\theta_{\text{out-of-ecliptic}}$ of the current-sheet normal vectors and will not affect low values of $\theta_{\text{out-of-ecliptic}}$: hence, the tilting of the flux tubes will reduce the average value of $\theta_{\text{out-of-ecliptic}}$.

Acknowledgments
The authors wish to thank Roberto Bruno, Len Fisk, Enrico Landi, Pete Riley, Ruth Skoug, John Steinberg, and Dan Welling for helpful conversations. This work was supported at the Space Science Institute by the NSF Solar-Terrestrial Program via grant AGS-1261659, by the NASA Heliophysics LWS TRT program via grants NNX14AN90G and NNX16AB75G, and by the NASA Heliophysics Guest Investigator Program via grant NNX14AC15G and supported at the University of Michigan by the NASA Geospace SR&T program via grant NNX12AD29G. ENLIL simulations were run at the Community Coordinated Modeling Center (CCMC) at NASA/Goddard Space Flight Center. All spacecraft data are available via the NASA data servers http://cdaweb.gsfc.nasa.gov, http://omniweb.gsfc.nasa.gov, and http://omniweb.gsfc.nasa.gov/coho/ and from the ACE data server http://www.srl.caltech.edu/ACE/ASC/. ENLIL simulation outputs are available at the CCMC server http://ccmc.gsfc.nasa.gov.

References

Adams, W. M. (1976), Differential rotation of photospheric magnetic fields associated with coronal holes, *Solar Phys.*, *47*, 601–605, doi:10.1007/BF00154768.

Arge, C. N., D. Odstrcil, V. J. Pizzo, and L. R. Mayer (2003), Improved method for specifying solar wind speed near the Sun, in *The Tenth International Solar Wind Conference*, pp. 190–193, AIP, Melville, New York.

Asbridge, J. R., S. J. Bame, W. C. Feldman, and M. D. Montgomery (1976), Helium and hydrogen velocity differences in the solar wind, *J. Geophys. Res.*, *81*, 2719–2727, doi:10.1029/JA081i016p02719.

Baker, D., L. van Driel-Gesztelyi, and G. R. R. Attril (2007), Evidence for interchange reconnection between a coronal hole and an adjacent emerging flux region, *Astron. Nachr.*, *328*, 773–776, doi:10.1002/asna.200710787.

Belcher, J. W., and L. Davis (1971), Large-amplitude Alfven waves in the interplanetary medium, 2, *J. Geophys. Res.*, *76*, 3534–3563, doi:10.1029/JA076i016p03534.

Borovsky, J. E. (2008), The flux-tube texture of the solar wind: Strands of the magnetic carpet at 1 AU?, *J. Geophys. Res.*, *113*, A08110, doi:10.1029/2007JA012684.

Borovsky, J. E. (2010), On the variations of the solar wind magnetic field about the Parker-spiral direction, *J. Geophys. Res.*, *115*, A09101, doi:10.1029/2009JA015040.

Borovsky, J. E. (2016), Plasma structure of the coronal-hole solar wind: Origins and Evolution, *J. Geophys. Res. Space Physics*, *121*, doi:10.1002/2016JA022686, in press.

Borovsky, J. E., and M. H. Denton (2006), The differences between CME-driven storms and CIR-driven storms, *J. Geophys. Res.*, *111*, A07S08, doi:10.1029/2005JA011447.

Borovsky, J. E., and M. H. Denton (2010a), On the heating of the outer radiation belt to produce high fluxes of relativistic electrons: Measured heating rates for high-speed stream-driven storms, *J. Geophys. Res.*, *115*, A12206, doi:10.1029/2010JA015342.

Borovsky, J. E., and M. H. Denton (2010b), The magnetic field at geosynchronous orbit during high-speed stream-driven storms: Connections to the solar wind, the plasma sheet, and the outer electron radiation belt, *J. Geophys. Res.*, *115*, A08217, doi:10.1029/2009JA015116.

Borovsky, J. E., and M. H. Denton (2010c), Solar wind turbulence and shear: A superposed-epoch analysis of corotating interaction regions at 1 AU, *J. Geophys. Res.*, *115*, A10101, doi:10.1029/2009JA014966.

Borovsky, J. E., and M. H. Denton (2013), The differences between storms driven by helmet-streamer CIRs and storms driven by pseudostreamer CIRs, *J. Geophys. Res. Space Physics*, *118*, 5506–5521, doi:10.1002/jgra.50524.

Borovsky, J. E., and S. P. Gary (2014), How important are the alpha-proton relative drift and the electron heat flux for the proton heating of the solar wind in the inner heliosphere? *J. Geophys. Res. Space Physics*, *119*, 5210–5219, doi:10.1002/2014JA019758.

Borrini, G., J. T. Gosling, S. J. Bame, W. C. Feldman, and J. M. Wilcox (1981), Solar wind helium and hydrogen structure near the heliospheric current sheet: A signal of coronal streamers at 1 AU, *J. Geophys. Res.*, *86*, 4565–4573, doi:10.1029/JA086iA06p04565.

Bruno, R., and B. Bavassano (1991), Origin of low cross-helicity regions in the inner solar wind, *J. Geophys. Res.*, *96*, 7841–7851, doi:10.1029/91JA00144.

Bruno, R., and V. Carbone (2013), The solar wind as a turbulence laboratory, *Living Rev. Solar Phys.*, *10*, 2, doi:10.12942/lrsp-2013-2.

Bruno, R., V. Carbone, P. Veltri, E. Pietropaolo, and B. Bavassano (2001), Identifying intermittency events in the solar wind, *Planet. Space Sci.*, *49*, 1201–1210, doi:10.1016/S0032-0633(01)00061-7.

Bruno, R., V. Carbone, L. Primavera, F. Malara, L. Sorriso-Valvo, B. Bavassano, and P. Veltri (2004), On the probability distribution function of small-scale interplanetary magnetic field fluctuations, *Ann. Geophys.*, *22*, 3751, doi:10.5194/angeo-22-3751-2004.

Burlaga, L. F. (1974), Interplanetary stream interfaces, *J. Geophys. Res.*, *25*, 3717–3725, doi:10.1029/JA079i025p03717.

Burlaga, L. F., and N. F. Ness (1969), Tangential discontinuities in the solar wind, *Solar Phys.*, *9*, 467–477, doi:10.1007/BF02391672.

Burlaga, L. F., W. H. Mish, and Y. C. Whang (1990), Coalescence of recurrent streams of different sizes and amplitudes, *J. Geophys. Res.*, *95*, 4247–4255, doi:10.1029/JA095iA04p04247.

Burton, M. E., M. Neugebauer, N. U. Crooker, R. von Steiger, and E. J. Smith (1999), Identification of trailing edge stream interfaces: A comparison of Ulysses plasma and composition measurements, *J. Geophys. Res.*, *104*, 9925–9932, doi:10.1029/1999JA900049.

Carovillano, R. L., and G. L. Siscoe (1969), Corotating structure in the solar wind, *Solar Phys.*, *8*, 401–414, doi:10.1007/BF00155388.

Close, R. M., C. E. Parnell, D. W. Longcope, and E. R. Priest (2004), Recycling of the solar corona's magnetic field, *Astrophys. J.*, *612*, L81–L84, doi:10.1086/424659.

Close, R. M., C. E. Parnell, D. W. Longcope, and E. R. Priest (2005), Coronal flux recycling times, *Solar Phys.*, *231*, 45–70, doi:10.1007/s11207-005-6878-1.

Crooker, N. U., and J. T. Gosling (1999), CIR morphology, turbulence, discontinuities, and energetic particles, *Space Sci. Rev.*, *89*, 179–220, doi:10.1023/A:1005253526438.

Crooker, N. U., and R. L. McPherron (2012), Coincidence of composition and speed boundaries of the slow solar wind, *J. Geophys. Res.*, *117*, A09104, doi:10.1029/2012JA017837.

Crooker, N. U., G. L. Siscoe, S. Shodhan, D. F. Webb, J. T. Gosling, and E. J. Smith (1993), Multiple heliospheric current sheets and coronal streamer belt dynamics, *J. Geophys. Res.*, *98*, 9371–9381, doi:10.1029/93JA00636.

Crooker, N. U., M. E. Burton, J. L. Phillips, E. J. Smith, and A. Balogh (1996), Heliospheric plasma sheets as small-scale transients, *J. Geophys. Res.*, *101*, 2426–2474.

Crooker, N. U., S. W. Kahler, J. T. Gosling, D. E. Larson, R. P. Lepping, E. J. Smith, and J. De Keyser (2001), Scales of heliospheric current sheet coherence between 1 and 5 AU, *J. Geophys. Res.*, *106*, 15,963–15,971, doi:10.1029/2000JA000109.

Crooker, N. U., E. M. Appleton, N. A. Schwadron, and M. J. Owens (2010), Suprathermal electron flux peaks at stream interfaces: Signature of solar wind dynamics or tracer for open magnetic flux transport on the Sun? *J. Geophys. Res.*, *115*, A11101, doi:10.1029/2010JA015496.

D'Amicis, R., G. Consolini, B. Bavassano, and R. Bruno (2012), Conditioned analysis of high-latitude solar wind intermittency, *Astrophys. J.*, *755*, 63,, 7, doi:10.1088/0004-637X/755/1/7.

Denton, M. H., J. E. Borovsky, R. M. Skoug, M. F. Thomsen, B. Lavraud, M. G. Henderson, R. L. McPherron, J. C. Zhang, and M. W. Liemohn (2006), Geomagnetic storms driven by ICME- and CIR-dominated solar wind, *J. Geophys. Res.*, *111*, A07S07, doi:10.1029/2005JA011436.

Ebert, R. W., M. A. Dayeh, M. I. Desai, and G. M. Mason (2012), Corotating interaction region associated suprathermal helium ion enhancements at 1 AU: Evidence for local acceleration at the compression region trailing edge, *Astrophys. J.*, *749*, 73, 13, doi:10.1088/0004-637X/749/1/73.

Elliott, H. A., D. J. McComas, N. A. Schwadron, J. T. Gosling, R. M. Skoug, G. Gloeckler, and T. H. Zurbuchen (2005), An improved expected temperature formula for identifying ICMEs, *J. Geophys. Res.*, *110*, A04103, doi:10.1029/2004JA010794.

Feldman, U., K. G. Widing, and H. P. Warren (1999), Morphology of the quiet solar upper atmosphere in the $4 \times 10^4 < T_e < 1.4 \times 10^6$ K temperature regime, *Astrophys. J.*, *522*, 1133–1147, doi:10.1086/307682.

Fisk, L. A., T. H. Zurbuchen, and N. A. Schwadron (1999a), Coronal hole boundaries and their interactions with adjacent regions, *Space Sci. Rev.*, *87*, 43–54, doi:10.1023/A:1005153730158.
Fisk, L. A., T. H. Zurbuchen, and N. A. Schwadron (1999b), On the coronal magnetic field: Consequences of large-scale motions, *Astrophys. J.*, *521*, 868–877, doi:10.1086/307556.
Forsyth, R. J., and E. Marsch (1999), Solar origin and interplanetary evolution of stream interfaces, *Space Sci. Rev.*, *89*, 7–20, doi:10.1023/A:1005235626013.
Freeman, J. W., and R. E. Lopez (1985), The cold solar wind, *J. Geophys. Res.*, *90*, 9885–9887, doi:10.1029/JA090iA10p09885.
Galvin, A. B., et al. (2008), The plasma and suprathermal ion composition (PLASTIC) investigation on the STEREO observatories, *Space Sci. Rev.*, *136*, 437–486, doi:10.1007/s11214-007-9296-x.
Geiss, J., G. Gloeckler, and R. von Steiger (1995), Origin of solar wind from composition data, *Space Sci. Rev.*, *72*, 49–60, doi:10.1007/BF00768753.
Gloeckler, G., et al. (1998), Investigation of the composition of solar and interstellar matter using solar wind and pickup ion measurements with SWICS and SWIMS on the ACE spacecraft, *Space Sci. Rev.*, *86*, 497–539, doi:10.1023/A:1005036131689.
Gloeckler, G., T. H. Zurbuchen, and J. Geiss (2003), Implications of the observed anticorrelation between solar wind speed and coronal electron temperature, *J. Geophys. Res.*, *108*(A4), 1158, doi:10.1029/2002JA009286.
Gosling, J. T., and V. J. Pizzo (1999), Formation and evolution of corotating interaction regions and their three dimensional structure, *Space Sci. Rev.*, *89*, 21–52, doi:10.1023/A:1005291711900.
Gosling, J. T., V. Pizzo, and S. J. Bame (1973), Anomalously low proton temperatures in the solar wind following interplanetary shock waves—Evidence for magnetic bottles, *J. Geophys. Res.*, *78*, 2001–2009, doi:10.1029/JA078i013p02001.
Gosling, J. T., J. R. Asbridge, S. J. Bame, and W. C. Feldman (1978), Solar wind stream interfaces, *J. Geophys. Res.*, *83*, 1401–1412, doi:10.1029/JA083iA04p01401.
Gosling, J. T., G. Borrini, J. R. Asbridge, S. J. Bame, W. C. Feldman, and R. T. Hansen (1981), Coronal streamers in the solar wind at 1 AU, *J. Geophys. Res.*, *86*, 5438–5448, doi:10.1029/JA086iA07p05438.
Gosling, J. T., D. N. Baker, S. J. Bame, W. C. Feldman, R. D. Zwickl, and E. J. Smith (1987), Bidirectional solar wind electron heat flux events, *J. Geophys. Res.*, *92*, 8519–8535, doi:10.1029/JA092iA08p08519.
Greco, A., W. H. Matthaeus, S. Servidio, P. Chuychai, and P. Dmitruk (2009), Statistical analysis of discontinuities in solar wind ACE data and comparison with intermittent MHD turbulence, *Astrophys. J.*, *691*, L111–L114, doi:10.1088/0004-637X/691/2/L111.
Hagenaar, H. J., C. J. Schriver, and A. M. Title (1997), The distribution of cell sizes of the solar chromosphere network, *Astrophys. J.*, *481*, 988–995, doi:10.1086/304066.
Hiremath, K. M., and M. Hedge (2013), Rotation rates of coronal holes and their probable anchoring depths, *Astrophys. J.*, *763*, 137, doi:10.1088/0004-637X/763/2/137.
Hirshberg, J., J. R. Asbridge, and D. E. Robbins (1974), The Helium component of solar wind velocity streams, *J. Geophys. Res.*, *79*, 934–938, doi:10.1029/JA079i007p00934.
Hundhausen, A. J. (1973), Nonlinear model of high-speed solar wind streams, *J. Geophys. Res.*, *78*, 1528–1542, doi:10.1029/JA078i010p01528.
Intriligator, D. S., J. R. Jokipii, T. S. Horbury, J. M. Intriligator, R. J. Forsyth, H. Kunow, G. Wibberenz, and J. T. Gosling (2001), Processes associated with particle transport in corotating interaction regions and near stream interfaces, *J. Geophys. Res.*, *106*, 10,625–10,634, doi:10.1029/2000JA000070.
Jian, L., C. T. Russell, J. G. Luhmann, and R. M. Skoug (2006), Properties of stream interactions at one AU during 1995–2004, *Solar Phys.*, *239*, 337–392, doi:10.1007/s11207-006-0132-3.
Kahler, S. (2010), A search for compositional differences in slow solar wind at the leading and trailing edges of stream interfaces, *AIP Conf. Proc.*, *216*, 383–386.
Kahler, S., P. Jibben, and E. E. DeLuca (2010), TRACE observations of changes in coronal hole boundaries, *Solar Phys.*, *262*, 135–147, doi:10.1007/s11207-010-9517-4.
Kasper, J. C., A. J. Lazarus, J. T. Steinberg, K. W. Ogilvie, and A. Szabo (2006), Physics-based tests to identify the accuracy of solar wind ion measurements: A case study with the Wind Faraday Cups, *J. Geophys. Res.*, *111*, A03105, doi:10.1029/2005JA011442.
King, J. H., and N. E. Papitashvili (2005), Solar wind spatial scales in and comparisons of hourly Wind and ACE plasma and magnetic field data, *J. Geophys. Res.*, *110*, A02104, doi:10.1029/2004JA010649.
Knetter, T., F. M. Neubauer, T. Horbury, and A. Balogh (2004), Four-point discontinuity observations using Cluster magnetic field data: A statistical survey, *J. Geophys. Res.*, *109*, A06102, doi:10.1029/2003JA010099.
Ko, Y.-K., J. C. Raymond, T. H. Zurbuchen, P. Riley, J. M. Raines, and L. Strachan (2006), Abundance variation at the vicinity of an active region and the coronal origin of slow solar wind, *Astrophys. J.*, *646*, 1275–1287, doi:10.1086/505021.
Kopp, R. A., G. Poletto, G. Noci, and M. Bruner (1985), Analysis of loop flows observed on 27 March, 1980 by the UVSP instrument during the Solar Maximum Mission, *Solar Phys.*, *98*, 91–118, doi:10.1007/BF00177201.
Krista, L. D., P. T. Gallagher, and D. S. Bloomfield (2011), Short-term evolution of coronal hole boundaries, *Astrophys. J. Lett.*, *731*, L26, doi:10.1088/2041-8205/731/2/L26.
Landi, E., R. L. Alexander, J. R. Gruesbeck, J. A. Gilbert, S. T. Lepri, W. B. Manchester, and T. H. Zurbuchen (2012), Carbon ionization stages as a diagnostic of the solar wind, *Astrophys. J.*, *744*, 100, doi:10.1088/0004-637X/744/2/100.
Lavraud, B., M. F. Thomsen, J. E. Borovsky, M. H. Denton, and T. I. Pulkkinen (2006), Magnetosphere preconditioning under northward IMF: Evidence from the study of coronal mass ejection and corotating interaction region geoeffectiveness, *J. Geophys. Res.*, *111*, A09208, doi:10.1029/2005JA011566.
Lazarus, A., J. Kasper, A. Szabo, and K. Ogilvie (2003), Solar wind streams and their origins, *AIP Proc.*, *679*, 187–189.
Lepping, R. P., et al. (1995), The Wind magnetic field investigation, *Space Sci. Rev.*, *71*, 207–229, doi:10.1007/BF00751330.
Lepping, R. P., C.-C. Wu, and D. B. Berdichevsky (2005), Automatic identification of magnetic cloud-like regions at 1 AU: Occurrence rate and other properties, *Ann. Geophys.*, *23*, 2687–2704, doi:10.5194/angeo-23-2687-2005.
Lin, R. P., et al. (1995), A three-dimensional plasma and energetic particle investigation for the WIND spacecraft, *Space Sci. Rev.*, *71*, 125–153, doi:10.1007/BF00751328.
Lucek, E. A., and A. Balogh (1998), The identification and characterization of Alfvenic fluctuations in ULYSSES data at midlatitudes, *Astrophys. J.*, *507*, 984–990, doi:10.1086/306372.
Mariani, F., B. Bavassano, and U. Villante (1983), A statistical study of MHD discontinuities in the inner solar system: Helios 1 and 2, *Solar Phys.*, *83*, 349–365, doi:10.1007/BF00148285.
Marsch, E., K.-H. Muhlhauser, H. Rosenbauer, R. Schwenn, and F. M. Neubauer (1982), Solar wind helium ions: Observations of the Helios solar probes between 0.3 and 1 AU, *J. Geophys. Res.*, *87*, 35–51, doi:10.1029/JA087iA01p00035.

McComas, D. J., S. J. Blame, P. Barker, W. C. Feldman, J. L. Phillips, P. Riley, and J. W. Griffee (1998), Solar wind Electron Proton Alpha Monitor (SWEPAM) for the Advanced Composition Explorer, *Space Sci. Rev.*, *86*, 563–612, doi:10.1023/A:1005040232597.
McCracken, K. G., and N. F. Ness (1966), The collimation of cosmic rays by the interplanetary magnetic field, *J. Geophys. Res.*, *71*, 3315–3318, doi:10.1029/JZ071i013p03315.
McPherron, R. L., and J. Weygand (2006), The solar wind and geomagnetic activity as a function of time relative to corotating interaction regions, in *Recurrent Magnetic Storms*, edited by B. Tsurutani et al., 125 pp., AGU, Washington, D. C.
McPherron, R. L., D. N. Baker, and N. U. Crooker (2009), Role of the Russell-McPherron effect in the acceleration of relativistic electrons, *J. Atmos. Sol. Terr. Phys.*, *71*, 1032–1044, doi:10.1016/j.jastp.2008.11.002.
Nakagawa, T. (1993), Solar source of the interplanetary planar magnetic structures, *Solar Phys.*, *147*, 169–197, doi:10.1007/BF00675493.
Nakagawa, T., A. Nishida, and T. Saito (1989), Planar magnetic structures in the solar wind, *J. Geophys. Res.*, *94*, 11,761–11,775, doi:10.1029/JA094iA09p11761.
Nash, A. G., N. R. Sheeley, and Y.-M. Wang (1988), Mechanisms for the rigid rotation of coronal holes, *Solar Phys.*, *117*, 359–389, doi:10.1007/BF00147253.
Navarro-Peralta, P., and A. Sanchez-Ibarra (1994), An observational study of coronal hole rotation over the sunspot cycle, *Solar Phys.*, *153*, 169–178, doi:10.1007/BF00712499.
Neugebauer, M., and J. Giacalone (2010), Progress in the study of interplanetary discontinuities, *AIP Conf. Proc.*, *1216*, 194.
Ogilvie, K. W., et al. (1995), SWE, a comprehensive plasma instrument for the WIND spacecraft, *Space Sci. Rev.*, *71*, 55–77, doi:10.1007/BF00751326.
Odstrcil, D. (2003), Modeling 3-D solar wind structure, *Adv. Space Res.*, *32*, 497.
Owens, M. J., R. T. Wicks, and T. S. Horbury (2011), Magnetic discontinuities in the near-Earth solar wind: Evidence of in-transit turbulence or remnants of coronal structure?, *Solar Phys.*, *269*, 411–420, doi:10.1007/s11207-010-9695-0.
Pagel, A. C., N. U. Crooker, T. H. Zurbuchen, and J. T. Gosling (2004), Correlation of solar wind entropy and oxygen ion charge state ratio, *J. Geophys. Res.*, *109*, A01113, doi:10.1029/2003JA010010.
Pizzo, V. (1989), The evolution of corotating stream fronts near the ecliptic plane in the inner solar system, 1. Two dimensional fronts, *J. Geophys. Res.*, *94*, 8673–8684, doi:10.1029/JA094iA07p08673.
Pizzo, V. J. (1991), The evolution of corotating stream fronts near the ecliptic plane in the inner solar system: 2. Three-dimensional tilted-dipole fronts, *J. Geophys. Res.*, *96*, 5405–5420, doi:10.1029/91JA00155.
Reale, F. (2014), Coronal loops: Observations and modeling confined plasmas, *Living Rev. Solar Phys.*, *11*, 4, doi:10.12942/lrsp-2014-4.
Richardson, I. G. (1985), Low energy ions in co-rotating interaction regions at 1 AU: Evidence for statistical ion acceleration, *Planet. Space Sci.*, *33*, 557–569, doi:10.1016/0032-0633(85)90097-2.
Richardson, I. G., and H. V. Cane (2010), Near-Earth interplanetary coronal mass ejections during solar cycle 23 (1996–2009): Catalog and summary of properties, *Solar Phys.*, *264*, 189–237, doi:10.1007/s11207-010-9568-6.
Richardson, I. G., et al. (2006), Major geomagnetic storms ($Dst \leq -100$ nT) generated by corotating interaction regions, *J. Geophys. Res.*, *111*, A07S09, doi:10.1029/2005JA011273.
Richter, A. K., and A. H. Luttrell (1986), Superposed epoch analysis of corotating interaction regions at 0.3 and 1.0 AU: A comparative study, *J. Geophys. Res.*, *91*, 5873–5878, doi:10.1029/JA091iA05p05873.
Schrijver, C. J. (2007), Braiding-induced interchange reconnection of the magnetic field and the width of solar coronal loops, *Astrophys. J.*, *662*, L119–L122, doi:10.1086/519455.
Schrijver, C. J., A. M. Title, A. A. van Ballegooijen, H. J. Hagenaar, and R. A. Shine (1997), Sustaining the quiet photospheric network: The balance of emergence, fragmentation merging, and cancellation, *Astrophys. J.*, *487*, 424–436, doi:10.1086/304581.
Sheeley, N. R., Jr. (1980), Temporal variation of loop structures in the solar atmosphere, *Solar Phys.*, *66*, 79–87, doi:10.1007/BF00150520.
Simon, G. W., and R. B. Leighton (1964), Velocity fields in the solar atmosphere. III. Large-scale motion, the chromospheric network, and magnetic fields, *Astrophys. J.*, *140*, 1120, doi:10.1086/148010.
Simunac, K. D. C., et al. (2009), In situ observations of solar wind stream interface evolution, *Solar Phys.*, *259*, 323, doi:10.1007/s11207-009-9393-y.
Simunac, K. D. C., A. B. Galvin, J. Barry, C. Farrugia, L. M. Kistler, H. Kucharek, M. A. Lee, Y. C.-M. Liu, E. Mobius, and M. A. Popecki (2010), Identifying the ends of high-speed streams near 1 AU with in situ data from STEREO/PLASTIC, *AIP Conf. Proc.*, *216*, 351.
Siscoe, G., and D. Intriligator (1993), Three views of two giant streams: Aligned observations at 1 AU, 4.6 AU, and 5.9 AU, *Geophys. Res. Lett.*, *20*, 2267–2270, doi:10.1029/93GL02488.
Siscoe, G. L., B. Goldstein, and A. J. Lazarus (1969), An east-west asymmetry in the solar wind velocity, *J. Geophys. Res.*, *74*, 1759–1762, doi:10.1029/JA074i007p01759.
Smith, C. W., M. H. Acuna, L. F. Burlaga, J. L'Heureux, N. F. Ness, and J. Scheifele (1998), The ACE magnetic fields experiment, *Space Sci. Rev.*, *86*, 611–632, doi:10.1023/A:1005092216668.
Smith, R. K., and J. P. Hughes (2010), Ionization equilibrium timescales in collisional plasmas, *Astrophys. J.*, *718*, 583–585, doi:10.1088/0004-637X/718/1/583.
Solomon, S. C., A. G. Burns, B. A. Emery, M. G. Mlynczak, L. Qian, W. Wang, D. R. Weimer, and M. Wiltberger (2012), Modeling studies of the impact of high-speed streams and corotating interaction regions on the thermosphere-ionosphere, *J. Geophys. Res.*, *117*, A00L11, doi:10.1029/2011JA017417.
Srikanth, R., J. Singh, and K. P. Raju (2000), Distribution of supergranule sizes, *Astrophys. J.*, *534*, 1008–1019, doi:10.1086/308777.
Subramanian, S., M. S. Madjarska, and J. G. Doyle (2010), Coronal hole boundaries evolution at small scales II. XRT view. Can small-scale outflows at CHBs be a source of the slow wind?, *Astron. Astrophys.*, *516*, A50, doi:10.1051/0004-6361/200913624.
Tessein, J. A., C. W. Smith, B. J. Vasquez, and R. M. Skoug (2011), Turbulence associated with corotating interaction regions at 1 AU: Inertial and dissipation rage magnetic field spectra, *J. Geophys. Res.*, *116*, A10104, doi:10.1029/2011JA016647.
Timothy, A. F., A. S. Krieger, and G. S. Vaiana (1975), The structure and evolution of coronal holes, *Solar Phys.*, *42*, 135–156, doi:10.1007/BF00153291.
Tsurutani, B. T., and C. M. Ho (1999), A review of discontinuities and Alfven waves in interplanetary space: ULYSSES results, *Rev. Geophys.*, *37*, 517–541, doi:10.1029/1999RG900010.
Tsurutani, B. T., W. D. Gonzalez, A. L. C. Gonzalez, F. Tang, J. K. Arballo, and M. Okada (1995), Interplanetary origin of geomagnetic activity in the declining phase of the solar cycle, *J. Geophys. Res.*, *100*, 21,717–21,733, doi:10.1029/95JA01476.
Tsurutani, B., R. McPherron, W. Gonzalez, G. Lu, J. H. A. Sobral, and N. Goalswamy (Eds.) (2006), *Recurrent Magnetic Storms*, AGU, Washington, D. C.
Tu, C.-Y., and E. Marsch (1995), MHD structures, waves and turbulence in the solar wind, *Space Sci. Rev.*, *73*, 1–210, doi:10.1007/BF00748891.
Vasquez, B. J., and J. V. Hollweg (1999), Formation of pressure-balanced structures and fast waves from nonlinear Alfven waves, *J. Geophys. Res.*, *104*, 4681–4696, doi:10.1029/1998JA900090.

Viall, N. M., and J. A. Klimchuk (2011), Patterns of nanoflare storm heating exhibited by an active region observed with Solar Dynamics Observatory/Atmosphere Imaging Assembly, *Astrophys. J.*, *738*, 24, 10, doi:10.1088/0004-637X/738/1/24.

Wang, Y.-M., and N. R. Sheeley (2004), Footpoint switching and the evolution of coronal holes, *Astrophys. J.*, *612*, 1196–1205, doi:10.1086/422711.

Wimmer-Schweingruber, R. R., R. von Steiger, and R. Paerli (1997), Solar wind stream interfaces in corotating interaction regions: SWICS/Ulysses results, *J. Geophys. Res.*, *102*, 17,407–17,417, doi:10.1029/97JA00951.

Xu, F., and J. E. Borovsky (2015), A new four-plasma categorization scheme for the solar wind, *J. Geophys. Res. Space Physics*, *120*, 70–100, doi:10.1002/2014JA020412.

Yang, S., J. Zhang, T. Li, and Y. Liu (2011), SDO observations of magnetic reconnection at coronal hole boundaries, *Astrophys. J. Lett.*, *732*, L7, 6, doi:10.1088/0004-637X/732/1/15.

Zhao, L., T. H. Zurbuchen, and L. A. Fisk (2009), Global distribution of the solar wind during solar cycle 23: ACE observations, *Geophys. Res. Lett.*, *36*, L14104, doi:10.1029/2009GL039181.

Zhdankin, V., S. Boldyrev, J. Mason, and J. C. Perez (2012), Magnetic discontinuities in magnetohydrodynamic turbulence and in the solar wind, *Phys. Rev. Lett.*, *108*, 175004, doi:10.1103/PhysRevLett.108.175004.

Zirker, J. B. (1977), Coronal holes and high-speed wind streams, *Rev. Geophys. Space Phys.*, *15*, 257–269, doi:10.1029/RG015i003p00257.

Zurbuchen, T. H., S. Hefti, L. A. Fisk, G. Gloeckler, and R. von Steiger (1999), The transition between fast and slow solar wind from composition data, *Space Sci. Rev.*, *87*, 353–356, doi:10.1023/A:1005126718714.